minerals

MDPI

Article

Lithofacies Characteristics and Sweet Spot Distribution of Lacustrine Shale Oil Reservoirs: A Case Study of the Second Member of the Kongdian Formation in the Cangdong Sag, Bohai Bay Basin

Yuan Zhan [1,2,*], Chengyan Lin [1,2,*], Cunfei Ma [1], Wenzhong Han [3], Pengjie Ma [4] and Guiang Li [1,2]

1 School of Geosciences, China University of Petroleum (East China), Qingdao 266580, China
2 National Key Laboratory of Deep Oil and Gas, China University of Petroleum (East China), Qingdao 266580, China
3 Research Institute of Exploration and Development, Dagang Oilfield Company, PetroChina, Tianjin 300280, China
4 Sanya Offshore Oil & Gas Research Institute, Northeast Petroleum University, Sanya 572025, China
* Correspondence: b18010020@s.upc.edu.cn (Y.Z.); lincy@upc.edu.cn (C.L.)

Abstract: In contrast to marine shale oil reservoirs, lacustrine shale exhibits rapid lithofacies changes and strong mineral compositional heterogeneity, posing new challenges for the evaluation and distribution prediction of shale oil sweet spots. The oiliness, reservoir properties, oil fluidity, and fracability of different lithofacies were analyzed using emission-scanning electron microscopy (FE-SEM) observation, low-pressure nitrogen physisorption (LNP) analysis, mercury intrusion porosimetry (MIP), nuclear magnetic resonance (NMR), and triaxial compression testing. Based on the mineral composition obtained from X-ray diffraction (XRD) analysis, total organic carbon (TOC) content, and sedimentary structure, four lithofacies were classified, which are organic-rich laminated calcareous shale (LC), organic-rich laminated siliceous shale (LS), organic-rich laminated mixed shale (LM), and organic-poor massive calcareous shale (MC). Considering the factors of oiliness, reservoir properties, oil fluidity, and fracability, the LC and LS lithofacies were determined as being high-quality sweet spots (type I). Within the stratigraphic sequence divided by GR-INPEFA curves, multi-resolution graph-based clustering (MRGC) analysis of sensitive well logs was used to classify the lithofacies, after which the distribution of sweet spots was predicted. The results reveal that the sweet spots exhibit regular changes in their vertical distribution and a ring-like pattern in their planar distribution, influenced by variations in the sedimentary environment. This finding can offer valuable guidance for the future exploitation of shale oil in the Guandong region.

Keywords: lacustrine shale; shale oil; lithofacies; sweet spot; Kongdian Formation; Cangdong Sag

check for updates

Citation: Zhan, Y.; Lin, C.; Ma, C.; Han, W.; Ma, P.; Li, G. Lithofacies Characteristics and Sweet Spot Distribution of Lacustrine Shale Oil Reservoirs: A Case Study of the Second Member of the Kongdian Formation in the Cangdong Sag, Bohai Bay Basin. *Minerals* **2023**, *13*, 1391. https://doi.org/10.3390/min13111391

Academic Editor: Leszek Marynowski

Received: 12 August 2023
Revised: 24 October 2023
Accepted: 28 October 2023
Published: 30 October 2023

Copyright: © 2023 by the authors. Licensee MDPI, Basel, Switzerland. This article is an open access article distributed under the terms and conditions of the Creative Commons Attribution (CC BY) license (https://creativecommons.org/licenses/by/4.0/).

1. Introduction

With the great success of the exploration and exploitation of marine shale reservoirs in North America, shale oil and gas have become an important target for exploitation globally, following conventional reservoirs [1,2]. After exploration and exploitation in recent years, Bohai Bay Basin in the east and the Ordos Basin and Jimsar Basin in the west of China have shown great shale oil and gas potential in the Miocene continental strata [3–5]. Differently from the large set of fine-grained deposits and relatively weak heterogeneity of marine shale reservoirs in North America, such as Barnett and Marcellus shale, the water body of the continental lacustrine basin changes quickly, and the lithofacies transition of shale reservoir is rapid, which both pose great challenges to the evaluation and prediction of shale oil sweet spots [6–8]. Therefore, it is becoming increasingly necessary to understand the heterogeneity of continental shale oil reservoirs and its influence on the comprehensive evaluation of sweet spots.

Due to the extremely poor physical properties of shale reservoirs and their special reservoiring characteristics of self-generation and self-storage, the fracturing engineering, oil generation potential of the source rock, and oil storage space should be considered in sweet spot evaluation [9–13]. Therefore, it is necessary to comprehensively evaluate shale oil reservoirs on the basis of four aspects: oil generation, reservoir physical properties, fluidity, and fracturing properties. Many scholars have conducted research on shale oil reservoir sweet spots based on factors such as mineral composition, organic geochemical characteristics, physical properties, and rock mechanics, predicting the distribution of shale oil sweet spots by integrating these parameters [14–16]. Among these factors, pore structure influences reservoir space and reservoir permeability. However, the study of pore characteristics is affected by the varying resolutions of the different measurement methods. The practical research challenge lies in how to integrate multiple approaches for comprehensive analysis. There is a wide variety of shale oil reservoir sweet spot classification schemes, and their applicability to reservoirs formed under different environments is an important issue. In sweet spot classification methods based on the combination of relevant parameters, reservoir genesis has not been effectively coupled with sweet spots [17]. Lithofacies, as rock composition units influenced by the combined effects of tectonic, sedimentary, and diagenetic processes, form the foundation for sweet spot evaluation and can serve as a guide for predicting sweet spot distribution [18–23]. Using mineral composition, total organic carbon (TOC) content, and sedimentary structures to classify shale lithofacies is a mature method [24–26]. The lithofacies prediction at both vertical and horizontal scales was accomplished by establishing the correlation between core data with well logs and seismic data [27,28]. Moreover, the lithofacies of fine-grained reservoirs change rapidly, and it is difficult for the resolution of traditional geophysical means to meet the requirements for fine prediction of sweet spots. Due to the variety of shale lithofacies and the less distinct electrical signal differences among them compared to conventional reservoirs, there are certain limitations encountered when attempting to accurately predict lithofacies based on well logs. In recent years, the trend of multidisciplinary integration has promoted the application of intelligent methods in the petroleum industry [29,30]. Based on well logs, machine learning techniques leverage the computational power of computers to rapidly and efficiently identify deep-level differences between different lithofacies. The utilization of intelligent methods for high-precision and efficient lithofacies clustering and prediction stands as a pivotal direction for the future development of shale reservoir research [31].

The second member of the Paleocene Kongdian shale formation in the Cangdong Sag of the Bohai Bay Basin exhibits a wide distribution, considerable thickness, and high organic matter content, indicating significant potential for shale oil exploration and exploitation. The initial deployment of horizontal wells in the upper 40–60 m sweet spot objective interval of the Ek_2 formation has yielded promising results. However, the controlling mechanism of lithofacies on sweet spots remains unclear, necessitating the use of lithofacies distribution to predict sweet spots in other intervals. Firstly, in the sequence analyzed according to the GR-INPEFA curve, the lithofacies were classified based on core observation, thin section observation, XRD analysis, scanning electron microscopy (SEM) observation, and other methods. All the core data were sourced from the coring wells G-A, G-B, and G-C. Rock pyrolysis experiments, low-pressure nitrogen physisorption (LNP) analysis, mercury intrusion porosimetry (MIP), nuclear magnetic resonance (NMR), and triaxial compression testing were carried out to study the resource potential, reservoir property potential, and engineering development potential of different lithofacies. By utilizing high-precision lithofacies identification and prediction results at both vertical and horizontal scales, sweet spot prediction was accomplished. The primary objectives of this study are (1) to conduct a comprehensive sweet spot evaluation based on four aspects—oil generation properties, reservoir physical properties, shale oil fluidity, and engineering brittleness—of different lithofacies and (2) to indicate the distribution of sweet spot areas through high-precision lithofacies identification and prediction at both vertical and horizontal scales, thereby providing guidance for subsequent shale oil development.

2. Geological Setting

The Huanghua Depression is located in the central part of the Bohai Bay Basin and is bounded by the Cangxian Uplift in the north and the Chengning Uplift in the south (Figure 1a). The Cangdong Sag is a typical complex fault basin in the Huanghua Depression. It starts from the Kongdian Uplift in the south, ends at the Dongguang Uplift in the north, and is bounded by Cangxian Uplift and Xuhei Uplift in the east and west, with Cangdong Fault and Xuxi Fault, respectively. The total area of the Cangdong Sag exceeds 4000 km^2 [32,33]. It consists of the Nanpi Slope in the south, Shenvsi Faulted Nose Belt in the west, Kongxi Slope in the north, Kongdian Structural Belt, and Kongdong Slope in the east (Figure 1b).

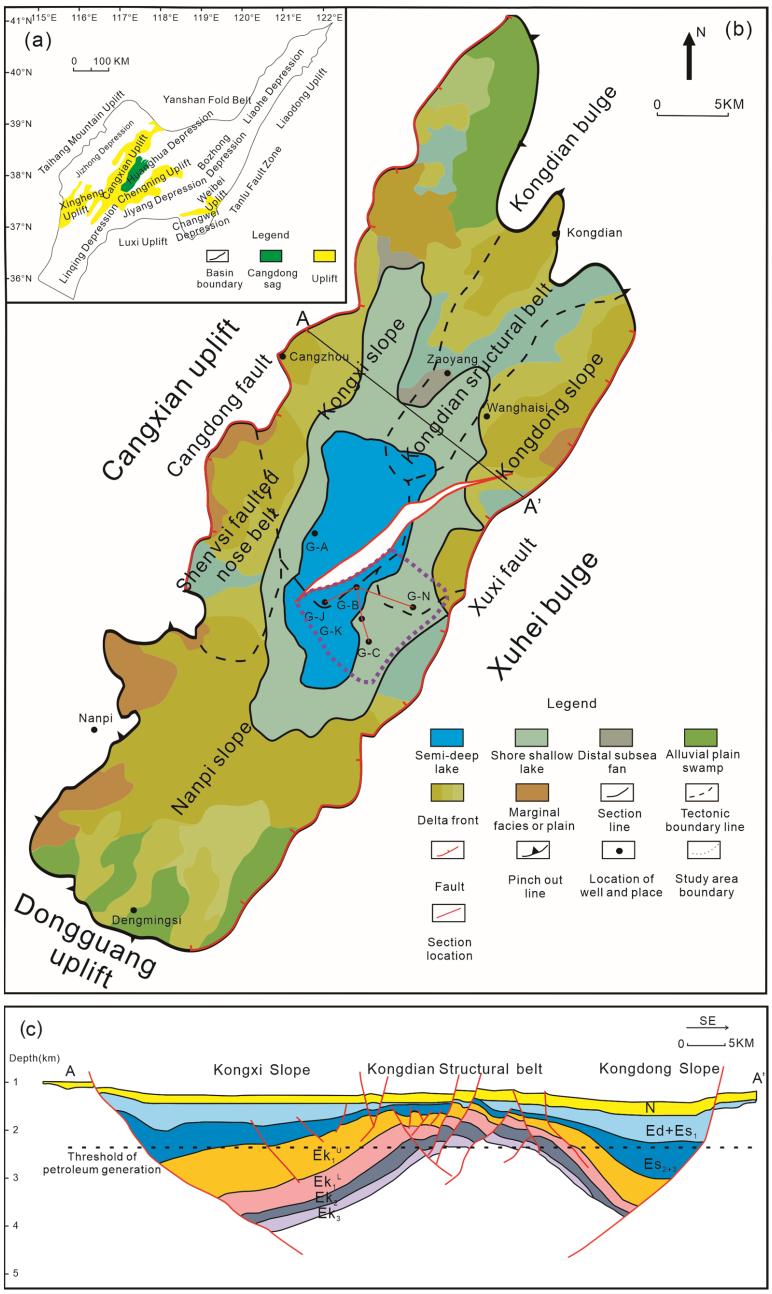

Figure 1. (**a**) Location of the Cangdong Sag in Bohai Bay Basin (modified after [34]). (**b**) Structural and sedimentary facies map of the regional setting of the Cangdong Sag (modified after [35]). (**c**) Typical sedimentary strata section of the Cangdong Sag (modified after [36,37]).

The Cangdong Sag developed in the regional extensional setting. In the Cangdong Sag, the Cenozoic strata include the Kongdian Formation, Shahejie Formation, Dongying Formation, Guantao Formation, and Minghuazhen Formation (Figure 2). In the Paleocene, the second member of the Kongdian Formation (Ek_2) deposited in the initial rift period was a semi-deep to deep lacustrine deposition, including a large and thick fine-grained sediment interval of 400–600 m. The burial depth of the second Kongdian Formation exceeds 2500 m, with the majority of the area situated below the oil generation threshold depth (Figure 1c). Ek_2 is a complete sequence that is divided into four parasequences from bottom to top: Ek_2^4, Ek_2^3, Ek_2^2, and Ek_2^1 [38,39]. The Ek_2^4 member is the fine sandstone and siltstone deposited in the delta sedimentary environment, while Ek_2^3–Ek_2^1 represent the fine-grained sedimentary segment in a semi-deep lake to deep lake environment [35]. This study focuses on the fine-grained sedimentary segment (Ek_2^3–Ek_2^1) located in the Guandong region, which is in the eastern part of the Cangdong Sag. As a pioneering development block for shale oil reservoirs, significant progress has been witnessed in the Guandong region. Since 2017, several horizontal wells developed in the Ek_2^1 fine-grained sedimentary segment, and sustained and stable industrial production has been achieved, which indicates the huge potential for shale oil development in the Cangdong Sag [40].

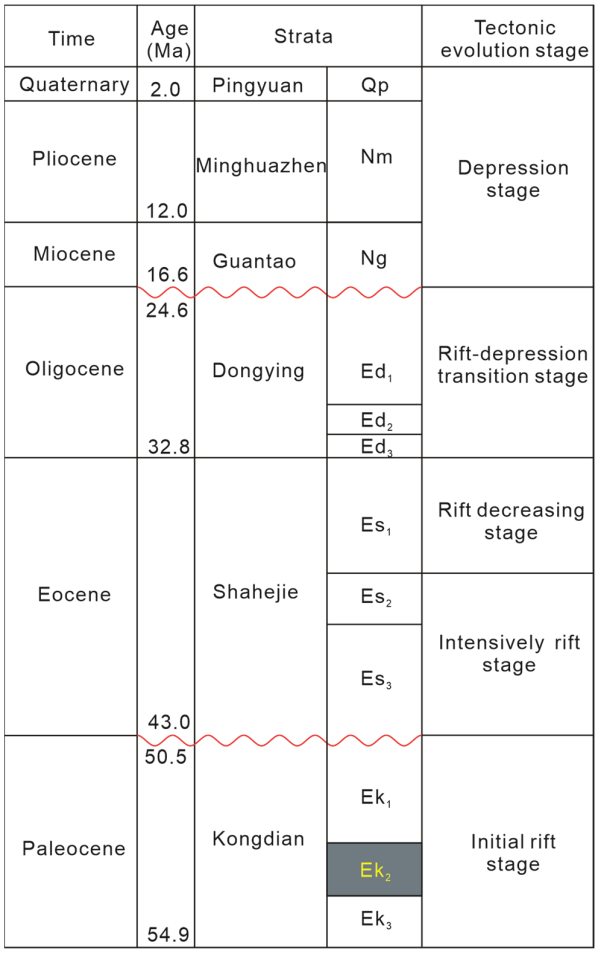

Figure 2. Stratigraphic column of the Cangdong Sag (modified after [41,42]).

3. Materials and Methods

The data for this study were collected from the fine-grained sedimentary interval of the Ek_2 formation in the wells G-A, G-B, and G-C. After a centimeter-level description of the core, more than 70 samples were collected for observation. All samples from different lithofacies were ground and polished into thin sections. In order to achieve clear observations of the organic matter morphology and internal structure, selected samples underwent

a 2 h argon ion polishing process using a LEICA EM TIC 3X instrument, with the polishing parameters set at 5 kV and 2 mA. Then, a Zeiss Axio Imager A2m optical microscope was used to take photographs. High-resolution imaging and analysis were performed on typical rock core thin sections using an FEI Quattro S Environmental Scanning electron microscope (ESEM) equipped with four energy dispersive X-ray spectroscopy (EDS, Oxford Ultim Max 40), Carl Zeiss Company, Oxford, United Kingdom. All photo analysis work was completed at the Research Institute of Exploration and Development of the Petrochina Dagang Oilfield Company and the Key Laboratory of Deep Oil and Gas of the China University of Petroleum (East China).

X-ray diffraction (XRD) analysis was carried out at the Key Laboratory of Deep Oil and Gas of the China University of Petroleum (East China). More than 1000 datasets from the wells G-A, G-B, and G-C were obtained using the X′Pert PRO MPD instrument with CuKα radiation. The instrument operated at a voltage of 40 kV and a current of 40 mA. The testing angle 2θ (mineral diffraction angle) range was set from 5° to 60°, and a sampling step size of 0.016° was used. The mass percentage of different minerals can be obtained by the computer of the diffraction pattern.

Tests on the chemical composition of organic matter were conducted at the Key Laboratory of Deep Oil and Gas of the China University of Petroleum (East China), and some data were collected from the Research Institute of Exploration and Development of the Petrochina Dagang Oilfield Company. The Leco CS-744 carbon–sulfur analyzer was used to combust the prepared 100-mesh powdered standard samples. The analysis strictly followed the TOC standard testing technique to obtain the total organic carbon content data for different lithological samples [43]. The free hydrocarbon (S_1; mg_{HC}/g_{rock}) and kerogen-derived hydrocarbon (S_2; mg_{HC}/g_{rock}) contents were analyzed using the Rock-Eval pyrolysis system (Rock-Eval7). The maximum hydrocarbon generation temperature (T_{max}) was recorded, and the hydrogen index (HI = $S_2 \times 100/TOC$; mg_{HC}/g_{TOC}) was calculated.

Low-pressure nitrogen physisorption (LNP) experiments were carried out on the Quantachrome NOVA 4200e analyzer in the Key Laboratory of Deep Oil and Gas of the China University of Petroleum (East China) (Qingdao, China). The sample was first crushed into 50-mesh-sized particles. After deoiling, drying at 110 °C for 10 h, and vacuum degassing at 110 °C for 24 h, the nitrogen adsorption experiment was conducted at −195 °C. The pore volume and pore size distribution were calculated according to the Barrett–Joyner–Halenda (BJH) method [44].

Mercury intrusion porosimetry (MIP) experiments were conducted using a Micromeritics Autopore IV 9500 V1.09 instrument at the Key Laboratory of Deep Oil and Gas of the China University of Petroleum (East China) in strict compliance with experimental operating standards. The pre-treated 1 cm^3 cubic samples were dried and then subjected to a mercury injection process. During the mercury injection process, the pressure was gradually increased up to 275 MPa, and then gradually reduced. The pore radius was calculated by recording the curve of mercury intake and removal. The MIP experiment can measure the pore size distribution in the range of 5.4 nm–200 μm.

Nuclear magnetic resonance (NMR) tests were performed at the Key Laboratory of Deep Oil and Gas of the China University of Petroleum (East China), using the MicroMR02-1 NMR core analyzer. Throughout the NMR experiment workflow, including reagent preparation, sample preparation, selection of measurement parameters, experimental execution, and data processing, there was rigorous adherence to industry standard requirements. The instrument operated under the conditions of 25 °C temperature, magnetic field strength of 0.3 T, and resonance frequency of 12 MHz. The detailed NMR experimental parameters included echo spacing of 0.25 ms, waiting time of 6000 ms, scan number of 128, and echo numbers of 4096. To eliminate the influence of kerogen and crystalline water on pore measurements, the standard core plug samples were subjected to drying and oil extraction. Subsequently, NMR measurements were taken of dried core, saturated water core, and centrifuged water core. The T_2 spectra of the samples in dry, saturation, and centrifugation

states were recorded using the Carr–Purcell–Meiboom–Gill (CPMG) sequence. The T_2 spectra were then analyzed to characterize the pore features of different samples.

Triaxial compression tests were conducted to test rock mechanical properties under simulated conditions of underground confining pressure. An RTR-1000 rock triaxial test system was used in the experimental device. The sample was a cylinder with a radius of 12.5 mm and a height of 50 mm. Under a confining pressure of 35 MPa, vertical pressure was applied until the rock was broken. The axial and radial displacements were, respectively, recorded by displacement sensors, and the stress–strain curves were obtained. Young's modulus and Poisson's ratio were calculated based on these curves. The experimental data were collected from the Research Institute of Exploration and Development of the Petrochina Dagang Oilfield Company.

Multi-resolution graph-based clustering (MRGC) is an unsupervised clustering algorithm that uses a multi-resolution clustering algorithm and well logging data as the basis to partition lithofacies [45]. The well logging phase recognition models of different lithofacies are established, and a KNN (K-nearest neighbor) algorithm is used to quickly and accurately classify lithofacies. For shale reservoirs, four sensitive well logs, including gamma ray (GR), acoustic transit time (AC), resistivity (RT), and total organic carbon (TOC) content, are selected for MRGC clustering. After the automatic clustering of lithofacies using the MRGC method, manual adjustments can be applied based on the core data. Ultimately, lithofacies–electrical relationship models are established for different lithofacies, enabling the rapid identification of lacustrine shale lithofacies based on conventional well logging data, and the approach is extended to all wells within the study area.

Since Wheeler introduced the concept of the reference plane, sequence stratigraphy has gradually become an important method in sedimentary research [46]. INPEFA technology can be used to identify the sedimentary cycle interface by integrating the difference between the maximum entropy spectrum analysis value and the conventional curve value and amplifying the subtle changes of typical well logs. Based on cyclic stratigraphy, the variation trend of the INPEFA curve that is calculated based on conventional logging curves can be used toward accurately understanding the formation development trend and ensuring a good correlation with the change in base level. The sequence stratigraphy, established using INPEFA technology, governs the sedimentary patterns of different lithofacies [47]. The GR log is strongly sensitive to mud content and was used to classify the sequence using INPEFA technology.

4. Results

4.1. Geochemical Characteristics, Petrology Characteristics, and Lithofacies Classification

4.1.1. Geochemical Characteristics

Under the control of parasequences reclassified according to the INPEFA curve, the geochemical parameter characteristics of the fine sediment member are obtained. The vitrinite reflectance (Ro) values of samples obtained from the entire fine-grained sedimentary member are consistently distributed within the range of 0.5 to 1, indicating that Ek_2^1–Ek_2^3 have all entered a mature stage of organic matter thermal evolution (Figure 3a). In Ek_2^1, the samples exhibit a wide range of TOC content, with values varying from 0.28 to 12.92 wt.%, with an average of 3.65 wt.%. The free and volatile hydrocarbons (S_1) values are distributed in the range of 0.10 to 8.36 mg_{HC}/g_{rock}, with an average of 0.58 mg_{HC}/g_{rock}. Additionally, the kerogen-derived hydrocarbon (S_2) values span from 0.2 to 72 mg_{HC}/g_{rock}, with an average of 23 mg_{HC}/g_{rock}. Moreover, the hydrogen index (HI) values range from 33 to 1327 mg_{HC}/g_{TOC}, with an average value of 559.8 mg_{HC}/g_{TOC}. The TOC of the Ek_2^2 samples ranges from 0.13 to 12.66 wt.%, with an average of 3.65 wt.%. The S_1 values are distributed in the range of 0.10 to 34 mg_{HC}/g_{rock}, with an average of 0.84 mg_{HC}/g_{rock}. Additionally, the S_2 values span from 0.10 to 69 mg_{HC}/g_{rock}, with an average of 14.04 mg_{HC}/g_{rock}. Moreover, the hydrogen index (HI) values range from 36 to 962 mg_{HC}/g_{TOC}, with an average value of 384.7 mg_{HC}/g_{TOC}. The TOC of the Ek_2^3 samples ranges from 0.15 to 12.47 wt.%, with an average of 4.09 wt.%. The S_1 values are distributed

in the range of 0.10 to 13.09 mg_{HC}/g_{rock}, with an average of 1.67 mg_{HC}/g_{rock}. Additionally, the S_2 values span from 0.19 to 67.14 mg_{HC}/g_{rock}, with an average of 21.91 mg_{HC}/g_{rock}. Moreover, the hydrogen index (HI) values range from 79.74 to 797 mg_{HC}/g_{TOC}, with an average value of 484.08 mg_{HC}/g_{TOC}.

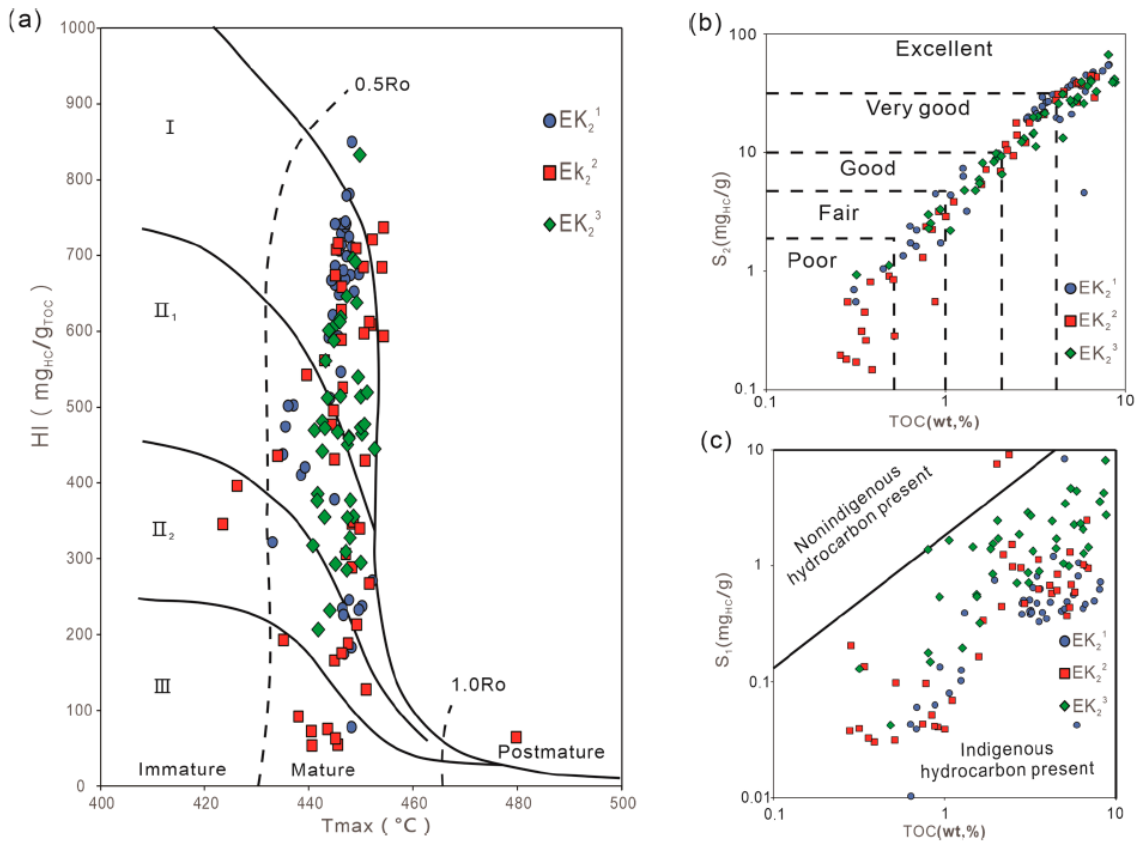

Figure 3. Geochemical parameters map of the Ek_2 shales in the Cangdong Sag. Crossplot of the (**a**) maximum hydrocarbon generation temperature (T_{max}) and hydrogen index (HI); (**b**) kerogen-derived hydrocarbons (S_2) and TOC; and (**c**) free and volatile hydrocarbons (S_1) and TOC.

The crossplot of T_{max} and HI shows that the kerogen of Ek_2^1 and Ek_2^3 is mainly type I and type II_1, and the kerogen of Ek_2^2 is type I, type II, and type III, with strong heterogeneity of kerogen [48]. The crossplot of TOC and S_2 shows that Ek_2^1 and Ek_2^3 samples have fair–excellent hydrocarbon generation potential [49]. The samples of Ek_2^2 show notable heterogeneity, with hydrocarbon generation potential ranging from poor to excellent (Figure 3b). The crossplot of TOC and S_1 (Figure 3c) shows that the samples of Ek_2^1–Ek_2^3 are all indigenous hydrocarbons [50].

4.1.2. Petrology Characteristics

Based on XRD analysis, in the Ek_2 fine-grained sedimentary member, the minerals, according to abundance from highest to lowest, are as follows: dolomite (0.0–95 wt.%, averaging 24.2 wt.%), feldspar (0.0–55 wt.%, averaging 19.4 wt.%), quartz (1.0–46 wt.%, averaging 17.5 wt.%), clay minerals (0.0–41 wt.%, averaging 14.8 wt.%), calcite (0.0–70 wt.%, averaging 14.5 wt.%), and analcime (0.0–59 wt.%, averaging 7.6 wt.%). Additionally, the minor presence of pyrite is observed, with an average proportion of 1.6 wt.%. In Ek_2, the dominant components of the siliceous fraction consist of quartz and feldspar particles derived from terrigenous detritus, with occasional occurrences of authigenic quartz (Figure 4a–c). These siliceous minerals predominantly exhibit a laminated appearance, interlayered with organic-rich clay minerals. Both dolomite and calcite predominantly occur as granular and micritic, often displaying layered distribution patterns (Figure 4d,e). Clay minerals are developed in intergranular pores of calcite and dolomite (Figure 4f).

The laminated structure of the Ek_2 member is constituted by organic-rich clay layers and other mineral layers (Figure 4g). Analcime is observed in various forms, such as clusters or dispersed particles, distributed throughout the entire Ek_2 formation (Figure 4h). Pyrite, identifiable under optical microscopy by its black color, exhibits relatively poor continuity, displaying a patchy distribution pattern (Figure 4i).

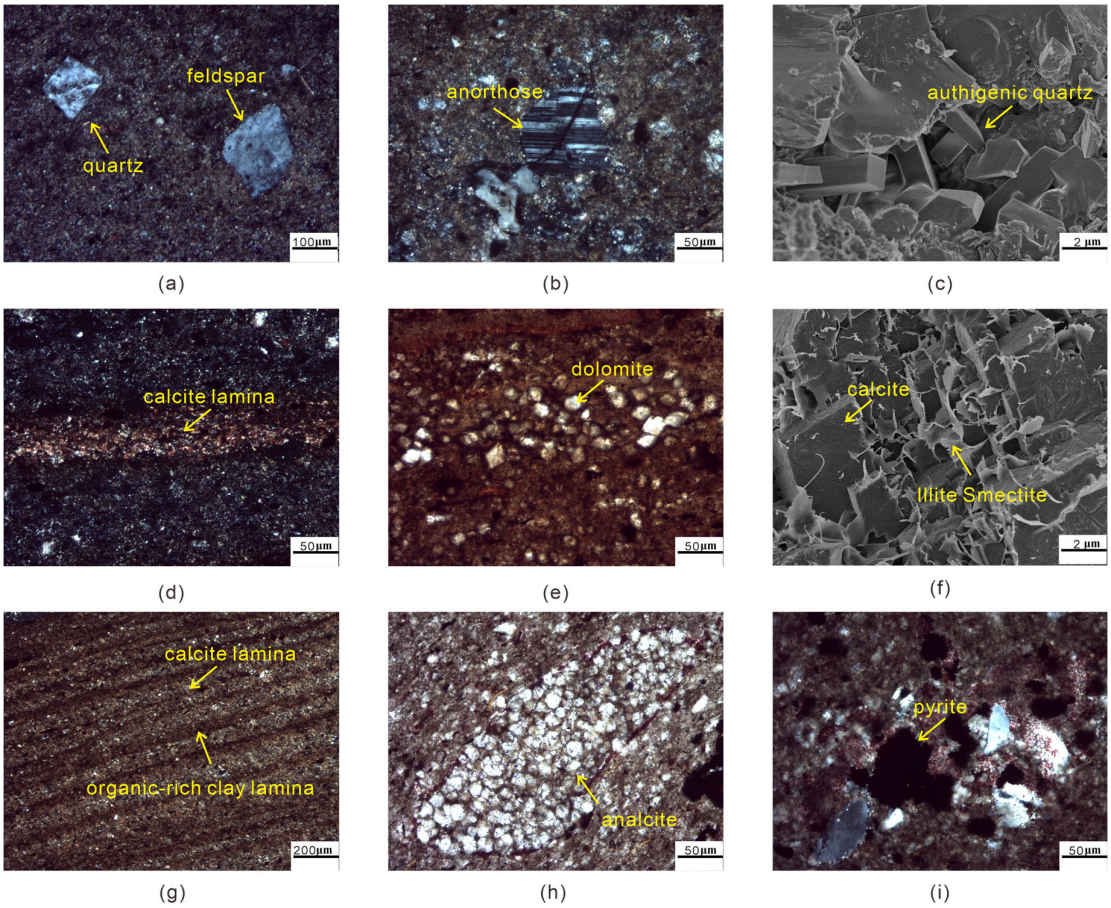

Figure 4. Mineral characteristics of the Ek_2 shale in the Cangdong Sag: (**a**) terrigenous quartz and feldspar particles (3201.14 m, G-A); (**b**) anorthose particles (3196.64 m, G-A); (**c**) authigenic quartz particles image from SEM (2992.79 m, G-A); (**d**) calcite lamina (3199.36 m, G-A); (**e**) dolomite lamina (3191.19 m, G-A); (**f**) SEM image of the fibrous clay minerals in the intergranular pores of calcite cement (3382.41 m, G-A); (**g**) interbedding of calcite laminae and organic-rich clay laminae (3199.36 m, G-A); (**h**) biogenic shell filled with analcite minerals (3194.59 m, G-A); (**i**) porphyritic pyrite in the matrix (3195.70 m, G-A).

From the vertical perspective, mainly calcareous shale and mixed shale developed in the Ek_2^1 formation, and mainly siliceous shale and mixed shale developed in the Ek_2^2 formation. All three lithologies are developed in the Ek_2^3 member, with the strongest heterogeneity observed in this formation.

The sedimentary structure of shale in the Ek_2 member is mostly laminated, and some of it is massive. The lamellar structure is developed in terms of siliceous shale, calcareous shale, and mixed shale, and the thickness of the lamina ranges between 1 μm and 1000 μm. The massive structures are mainly developed in calcareous shale.

4.1.3. Lithofacies Classification

Shale lithofacies can be classified into different types according to mineral composition, organic matter abundance, and sedimentary structure (Figures 5 and 6).

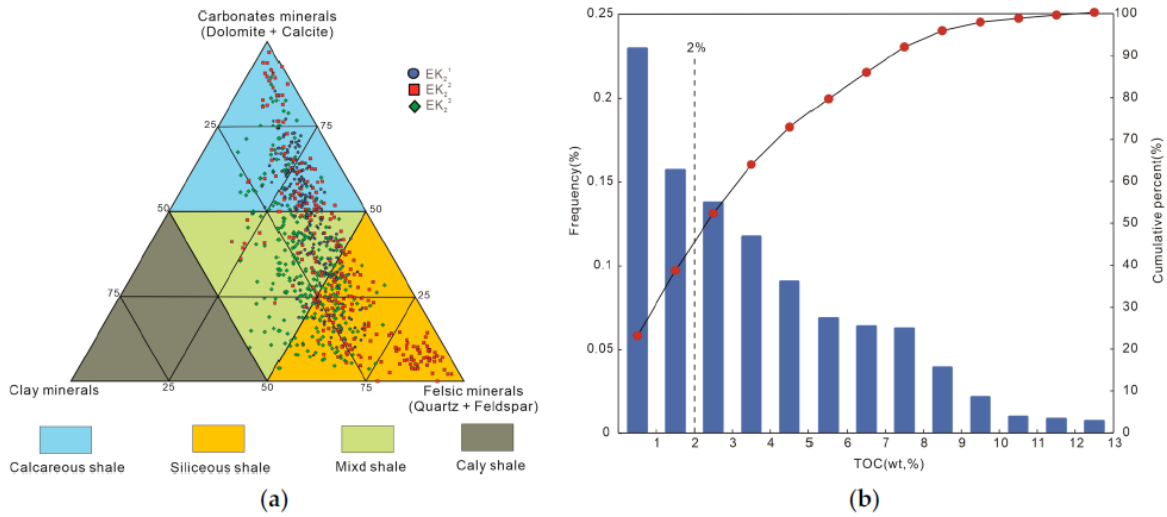

Figure 5. Classification of the Ek_2 shale in the Cangdong Sag: (**a**) ternary diagram of the mineral composition (modified after [51]); (**b**) histogram and cumulative distribution curve of the TOC.

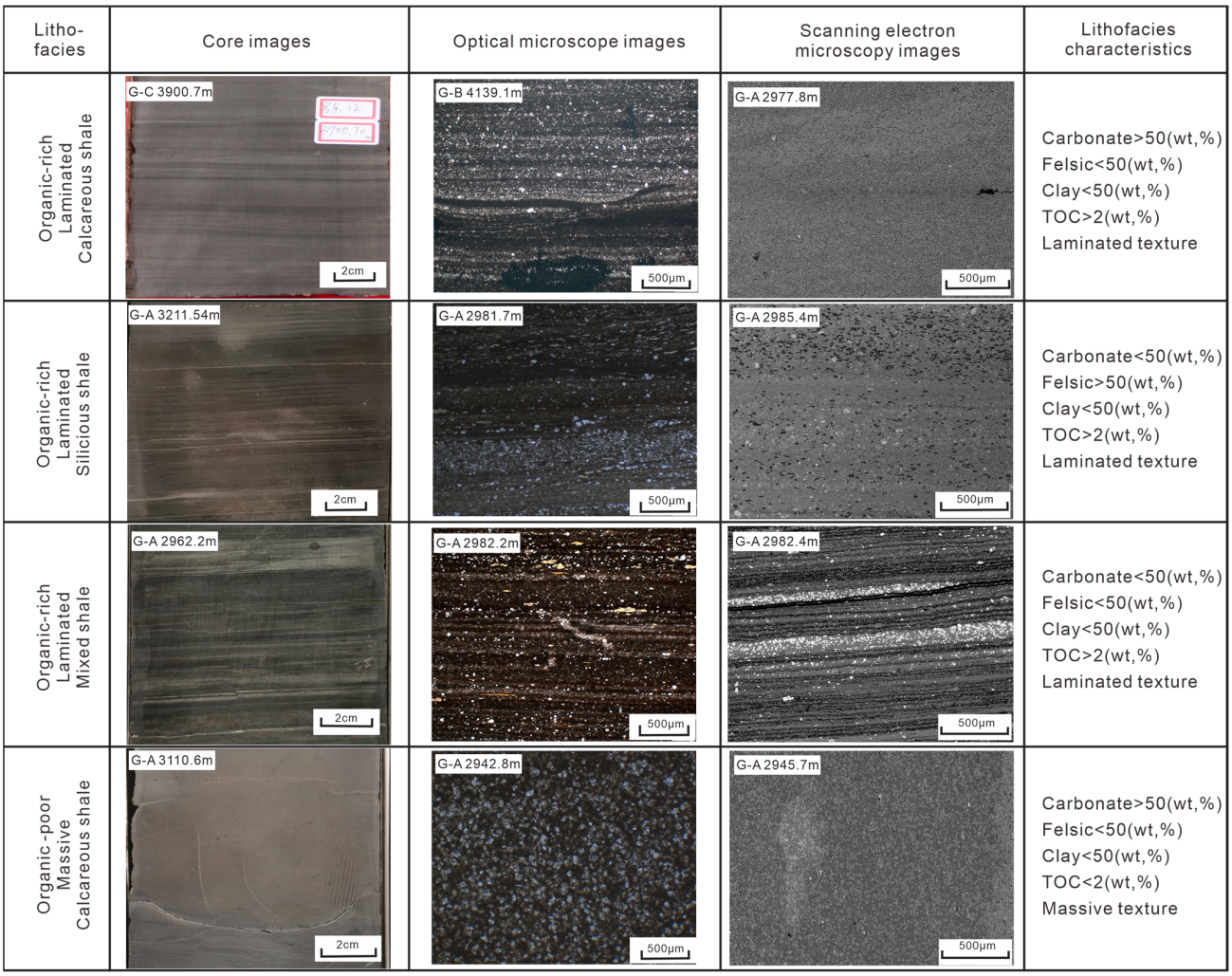

Figure 6. Lithofacies characteristics of the Ek_2 shale in the Cangdong Sag. Examples of each lithofacies shown as core photographs, thin section optical microscope images, scanning electron microscope images, and the mineral composition and structural characteristics.

The lithofacies of the Ek_2 member is classified into four categories based on mineral composition (with 50% as the threshold for determining the dominant lithology), organic matter content (with a TOC value of 2% as the threshold for assessing organic matter enrichment), and mineral compositional structure (laminated and massive features) (Figure 6).

Organic-rich laminated calcareous shale (LC). The organic carbon content exceeds 2 wt.%, the calcareous mineral content is more than 50 wt.%, the content of calcite is higher than that of dolomite, and the developed laminae are highly dense. The shade of color in the calcium-rich and organic-rich laminae varies, with distinct boundaries between the different types of laminae. Microscopic examination reveals oriented mineral arrangements with the development of bedding planes and fractures between the laminae.

Organic-rich laminated siliceous shale (LS). The organic carbon content exceeds 2 wt.%, the siliceous content is more than 50 wt.%, and the dominant laminae consist primarily of siliceous laminae and organic-rich laminae, with a minor occurrence of calcareous laminae. The core color is dark, and the laminae are continuous and straight. Microscopic examination reveals that the mineral arrangement is directional.

Organic-rich laminated mixed shale (LM). The organic carbon content exceeds 2 wt.%, and no dominant minerals are observed, as all mineral contents are less than 50 wt.%. Of these, clay minerals exhibited relatively higher proportions. The content of organic matter is high, and the color is the darkest among the four lithofacies. There is observed development of siliceous, calcareous, and organic-rich laminae, with indistinct boundaries between each type of laminae. Additionally, bedding plane fractures were found to be present between the laminae.

Organic-poor massive calcareous shale (MC). The organic carbon content is mostly less than 2 wt.%, and the calcareous mineral content is more than 50 wt.%. This lithofacies exhibits a massive structure, with dolomite as the predominant mineral composition, often featuring lens-shaped dolomite development. The core has a relatively light color and low organic matter content, and the microscopic observations reveal disordered mineral arrangements.

4.1.4. Vertical Variation in Lithofacies

Although lacustrine shales continuously deposit, their structure and mineral composition are not uniform. Influenced by the depositional environment, lacustrine shales exhibit certain regularities in both vertical and horizontal distributions. Therefore, under the control of sequence stratigraphy theory, it is essential to conduct lithofacies distribution studies within the sequenced framework delineated using the GR-INPEFA method. By utilizing the GR-INPEFA method and core XRD analysis, sequences $Ek_2{}^1$–$Ek_2{}^3$ were subdivided into seven parasequences from top to bottom, denoted as PS1 to PS7. Upon constructing the vertical lithofacies distribution diagrams for the three cored wells, it becomes evident that the lithofacies distribution characteristics are not same within different parasequences. Taking well G-A as an example (Figure 7a), PS1 is primarily characterized by LC lithofacies, with some occurrence of LS lithofacies. PS2 exhibits a tight sandstone distribution typical of nearshore subaqueous fans sedimentation. As the depth increases, the lithofacies of PS3 to PS5 transition gradually from the MC and LC lithofacies sedimentation to predominantly LS lithofacies sedimentation. In PS6 to PS7, all four lithofacies are present, with a notable abundance of LM lithofacies sedimentation.

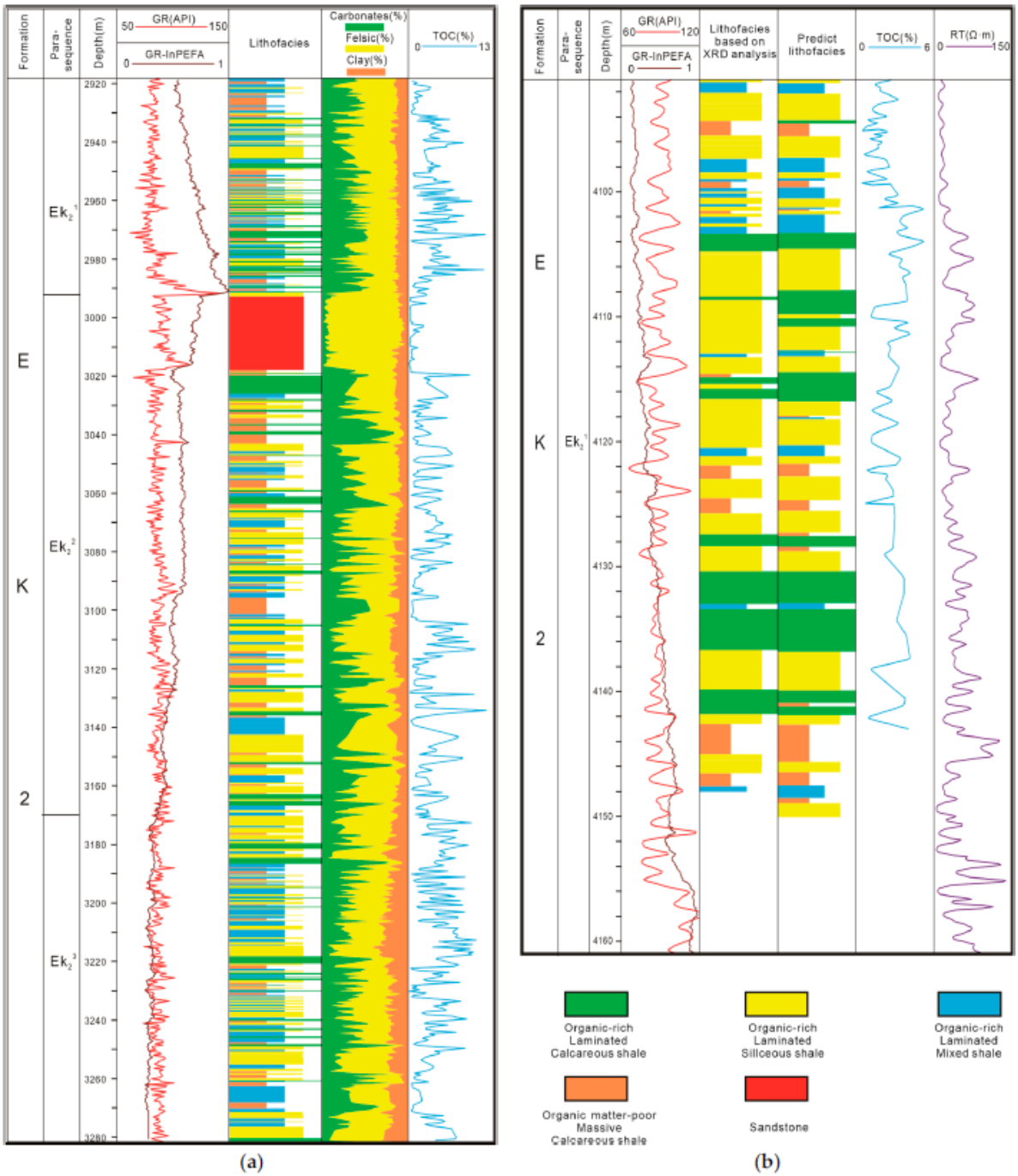

Figure 7. Well section for lithofacies classification and prediction: (**a**) well G-A; (**b**) well G-B.

4.2. Pore Structural Characteristics

4.2.1. Microscopic Pore Types

Given the self-generation and self-storage characteristics of shale oil reservoirs, coupled with the extremely poor physical properties, the development of pores and fractures serves as the primary storage space, becoming a crucial factor influencing shale oil storage and migration. According to the mudstone pore classification scheme, the pore system in the Ek_2 of the Cangdong Sag can be categorized into intergranular pores, intragranular pores, in addition to developed organic pores and microfractures [52]. Upon SEM observation of the samples, various minerals of different origins exhibit distinctive pore type characteristics. The pores within calcareous minerals predominantly encompass intercrystalline pores resulting from calcite recrystallization along with internal and external

dissolved pores and fractures, as well as intergranular pores occurring between dolomite grains (Figure 8a,b). Siliceous minerals are mainly intergranular pores contacted by quartz, feldspar, and other brittle minerals, mostly in narrow and long form (Figure 8c). Organic matter is highly abundant in the shale of the Ek_2 member in the study area. Organic matter pores and shrinkage fractures have developed in the process of thermal evolution, and the organic matter pores are mostly circular or irregular polygons (Figure 8d,e). The content of clay minerals is high in mixed shale. The clay minerals mainly develop intergranular pores, and shrinkage fractures form in the process of transformation and dehydration (Figure 8f,g). Pyrite deposition occurred in Ek_2 under an anaerobic reducing environment, with its intercrystalline pores exhibiting ribbon and irregular polygonal shapes (Figure 8h). In the study area, lamina development is pronounced across various lithofacies, and the contact surfaces between laminae composed of different minerals exhibit bedding plane fractures. These bedding plane fractures play a vital role in facilitating oil and gas migration and storage (Figure 8i). By acting as mechanical weak planes, these bedding plane fractures can form a network of fractures during subsequent hydraulic fracturing, thereby enhancing fracturing efficiency.

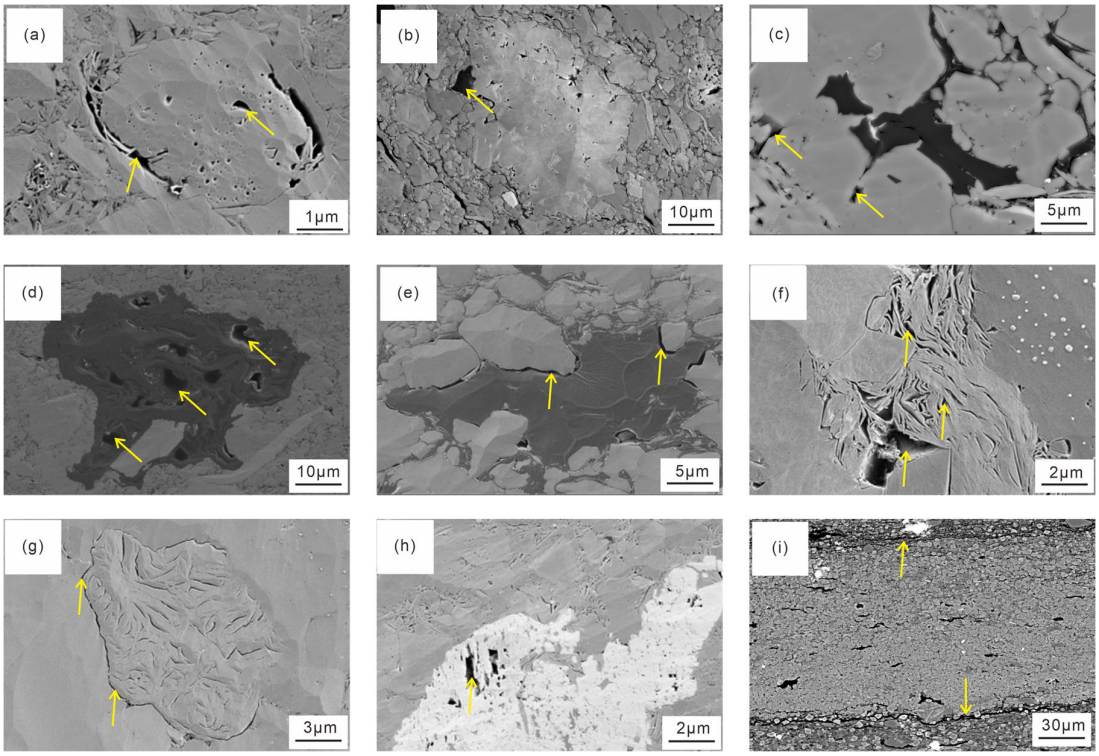

Figure 8. Typical pore characteristics of the Ek_2 shale in the Cangdong Sag: (**a**) calcite intragranular dissolved pores (2984.90 m, G-A); (**b**) dolomite intergranular pores (3085.50 m, G-A); (**c**) quartz intergranular pores (3032.50 m, G-A); (**d**) organic matter internal pores (2985.14 m, G-A); (**e**) organic matter shrinkage fractures (3123.20 m, G-A); (**f**) clay minerals intergranular pores (3116.81 m, G-A); (**g**) clay minerals shrinkage fractures (2987.37 m, G-A); (**h**) pyrite intercrystalline pores (2984.11 m, G-A); (**i**) bedding plane fractures of calcareous lamina (3014.2 m, G-A).

4.2.2. Microscopic Pore Structure Characteristics

LNP technology is a method to effectively characterize the distribution characteristics of micropores and mesopores by using the curves of N_2 adsorption capacity and pressure generated by nitrogen adsorption and desorption processes [53]. Based on the classification results of the LNP hysteresis loop according to IUPAC [54], the hysteresis loops of MC lithofacies samples are H2-type with a small amount of H4-type, indicating that the pore shape is primarily ink-bottle-type with a minor presence of narrow-slit-type (Figure 9a).

The hysteresis loops of the other laminated shale samples are H3-type, indicating that the pores are slit-like in shape. Moreover, the nitrogen adsorption capacity of MC lithofacies is significantly higher than that of other laminated shales, indicating that the massive shale has more developed micropores and mesopores than the laminated shale.

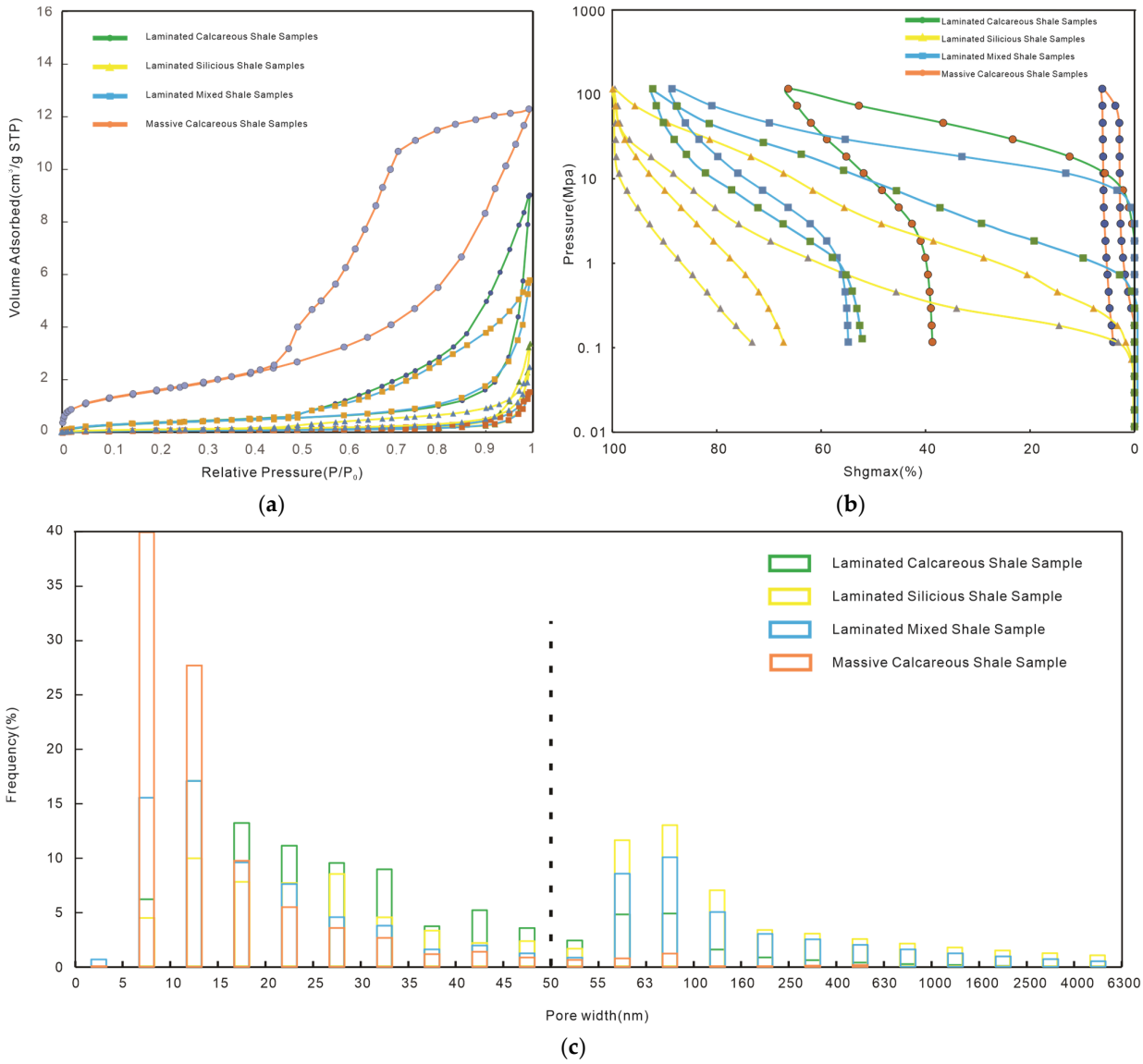

Figure 9. Pore structure characteristics measured by different methods of the Ek_2 shale in the Cangdong Sag: (**a**) low-pressure nitrogen physisorption; (**b**) mercury intrusion porosimetry. (**c**) The full-aperture distribution map.

Mercury intrusion porosimetry (MIP) requires recording the intrusion–extrusion volume of non-wetting phase mercury as a function of pressure increase and decrease to generate a function graph representing the relationship between the cumulative volume change of mercury and pressure. These plots are used to characterize the pore characteristics and connectivity of different lithofacies samples (Figure 9b). The study object of high-pressure mercury injection is nano-microscale pores. According to the characteristics of the mercury saturation–capillary pressure curves of the four lithofacies samples, MC shale has the lowest mercury-extrusion efficiency, and mercury extrusion is concentrated in the high-pressure stage, indicating there is a high proportion of micropores in the lithofacies. The pore characteristics of the three types of laminated shales also vary. LS shale and LM shale have the highest mercury intrusion and extrusion efficiency, and the mercury volume

increases at each pressure stage, indicating that both mesopores and macropores are well developed, and the pore connectivity is good. In contrast, LC shale has relatively few macropores, and mesopores are the predominant pores.

NMR can be used to detect information related to pore structure and the fluids within pores. The T_2 relaxation time distribution features can serve as a foundation for the analysis of pore size characteristics in different lithofacies samples (Figure 10). The signal morphology of the T_2 spectra of the dried sample represents solid organic matter, with the main relaxation time peaks of the four lithofacies falling between 0.1 and 1 ms. This pattern of T_2 spectra is consistent with the characteristics observed under saturated water conditions. The LM lithofacies exhibit larger-scale organic matter pores, which are attributed to the abundant occurrence of organic-rich laminae. After eliminating the influence of solid organic matter, analysis of the T_2 spectra under saturated water and centrifugation states was conducted. The T_2 spectral relaxation time of MC lithofacies presents a unimodal distribution, and the main peak is distributed at 0.8 ms, indicating that MC lithofacies mainly develop micropores and mesopores. The T_2 spectral relaxation time of the three laminated shales presents bimodal or trimodal distribution, with the left main peak developing around 0.8 ms and the right main peak developing between 10 ms and 1000 ms, indicating that mesopores and macropores are the predominant pore types in the laminated shales. The T_2 relaxation time of water-saturated shale samples can also be utilized to calculate the NMR porosity [55]. Among the four types of shales, LS lithofacies have the highest porosity (averaging 4.98%), followed by LC lithofacies (averaging 4.08%), and then LM lithofacies (averaging 3.44%), and MC lithofacies (averaging 2.08%) have the lowest porosity. The fluid signals of water saturation and centrifugation processes show that the MC lithofacies has the lowest mobile fluid saturation of the three laminated shales. LS and LM lithofacies have relatively higher mobile fluid saturation, followed by LC lithofacies, which is consistent with the mercury extrusion efficiency results of the MIP experiment.

LNP, MIP, and NMR experiments were used to characterize the pore structure at different scales, and the full-aperture distribution maps for four lithofacies in the fine-grained sedimentary part of Ek_2 were obtained (Figure 9c). Based on the IUPAC classification criteria, the pores can be classified as micropores (<2 nm), mesopores (2–50 nm), and macropores (>50 nm) [56]. It is worth emphasizing that, of the macropores larger than 50 nm, there are also microfractures with pore sizes exceeding 1 μm. Different experiments have varying measurement ranges for pore sizes. For instance, the LNP method typically measures pores in the range of 2 to 100 nm, whereas the MIP method is more accurate for pores in the range of 50 nm to 10 μm. Therefore, in this study, a comprehensive pore size characterization approach was adopted. For micropores and mesopores smaller than 50 nm, the LNP experiment results were used, whereas for larger pores and microfractures larger than 50 nm, the MIP test results were employed. Additionally, the qualitative control of pore size distribution characteristics was achieved through NMR analysis. The full-aperture distribution map reveals that mesopores dominate in different lithofacies of Ek_2, accounting for the largest proportion (54%–97%), followed by macropores and microfractures (up to 43%). The pore size distribution characteristics of different lithofacies exhibit pronounced heterogeneity. The peak pore size of MC lithofacies ranges from 5 nm to 15 nm, and there is little development of macropores. Among the three laminated shales, the peak pore size of LS lithofacies ranges from 55–100 nm, and macropores account for a large proportion. Mesopores of various sizes have developed in the LM lithofacies, and the distribution range of the main peaks is relatively wide, ranging from 5 to 25 nm, with a certain level of macropore development. The main peak of LC lithofacies is not obvious, and there is development of mesopores of various sizes. For all laminated shale lithofacies, there is the presence of a small number of pores with sizes exceeding 1000 nm, indicating the development of microfractures in addition to matrix pores.

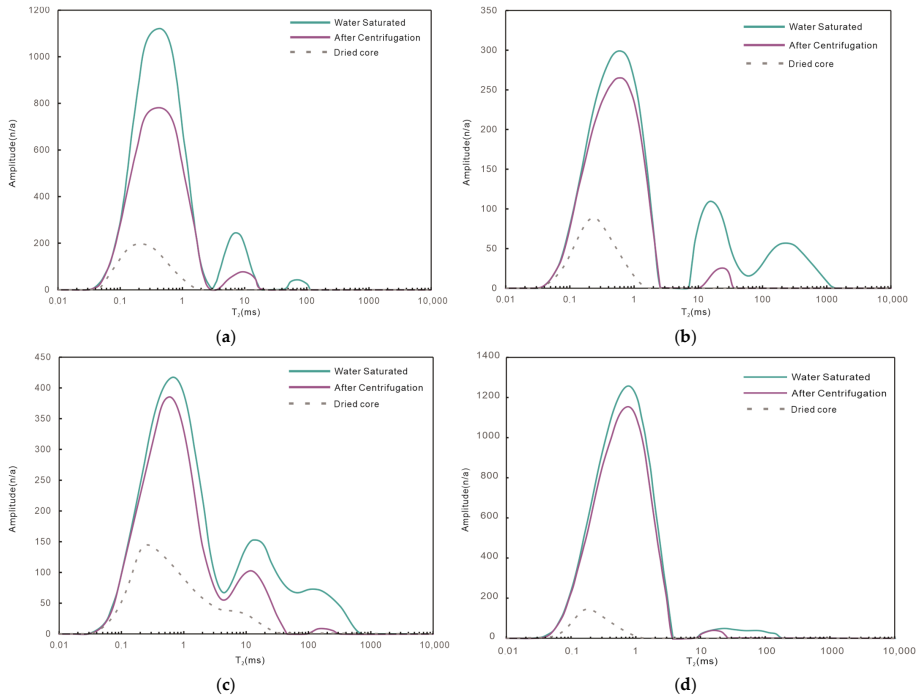

Figure 10. T_2 spectra from NMR experiments for different lithofacies: (**a**) organic-rich laminated calcareous shale; (**b**) organic-rich laminated siliceous shale; (**c**) organic-rich laminated mixed shale; (**d**) organic-poor massive calcareous shale.

4.3. Mechanical Fracturing Tests

Triaxial stress testing is a method to calculate Young's modulus and Poisson's ratio by applying different external forces to a sample under a certain confining pressure, monitoring the strain parameters and obtaining the stress–strain curve. The Young's modulus and Poisson's ratio are then used to further evaluate the brittleness of rock according to the classical mechanical parameter method with Equation (1). The mechanical parameters were obtained by conducting triaxial stress tests on 17 samples of the four shale lithofacies from Ek_2 at a confining pressure of 35 MPa. The accuracy of the mechanical brittleness index can be verified by comparison with the mineral brittleness index calculated by mineral composition content. The mineral brittleness index is calculated according to Equation (2) [57]:

$$BI_{mechanical} = \frac{E_{nor} + \mu_{nor}}{2} \times 100\% \tag{1}$$

$$BI_{minral} = \frac{V_{qua} + 0.3 \times V_{fel} + 0.5 \times V_{cal} + 0.7 \times V_{dol} + 0.5 \times V_{ana}}{V_{qua} + V_{fel} + V_{cal} + V_{dol} + V_{cla} + V_{ana} + V_{toc}} \times 100\% \tag{2}$$

where $BI_{mechanical}$ is the mechanical brittleness index; E_{nor} is the normalized Young's modulus; μ_{nor} is the normalized Poisson's ratio; $BI_{mineral}$ is the mineral brittleness index; V_{qua} is the volume fraction of the normalized quartz; V_{fel} is the volume fraction of the normalized feldspar; V_{cal} is the volume fraction of the normalized calcite; V_{dol} is the volume fraction of the normalized dolomite; V_{cla} is the volume fraction of the normalized clay; V_{ana} is the volume fraction of the normalized analcite; V_{toc} is the volume fraction of the normalized total organic carbon.

The mechanical parameters, along with the mineral composition data (from XRD analysis), are presented in Table 1. The results show that the LC and MC lithofacies have higher average Young's moduli (25.13 MPa and 26 MPa, respectively) and lower average Poisson's ratios (0.24 and 0.19, respectively). The average Young's moduli of the LS and LM lithofacies are relatively low (18.12 MPa and 19.77 MPa, respectively), and the average Poisson's ratios are higher (0.28 and 0.26, respectively). The mechanical brittleness index

values of four kinds of lithofacies increase in the following order: MC lithofacies (53.09), LC lithofacies (43.33), LM lithofacies (34.33), and LS lithofacies (31.37). Consequently, it can be inferred that calcareous shale exhibits good brittleness, while siliceous shale and mixed shale demonstrate relatively lower brittleness.

4.4. Lithofacies Prediction

Compared with conventional reservoirs, the lithofacies mineral composition of shale reservoirs is complex and changeable, and the difficulty of lithofacies identification and classification is greatly increased. After preprocessing and standardization of the well logging curves, four conventional well logging curves, natural gamma ray (GR), acoustic transit time (AC), resistivity (RT), and total organic carbon (TOC) content data were selected as input curves. The MRGC method was then employed to establish the well logging facies and lithofacies identification models for the four lithofacies in Ek_2. By comparison with the lithofacies prediction results for $EK_2{}^1$ in well G-B obtained using the MRGC technique with the lithofacies results from the XRD mineral identification, the accuracy rate is over 90%, indicating the favorable applicability of the MRGC technique for lithofacies identification in the Ek_2 (Figure 7b). Based on the lithofacies prediction results from all wells in the study area, two lithofacies well sections were constructed in the east–west and north–south directions (Figure 11). The analysis revealed significant regularities in the vertical and horizontal aspects of lithofacies distribution in the Guandong region.

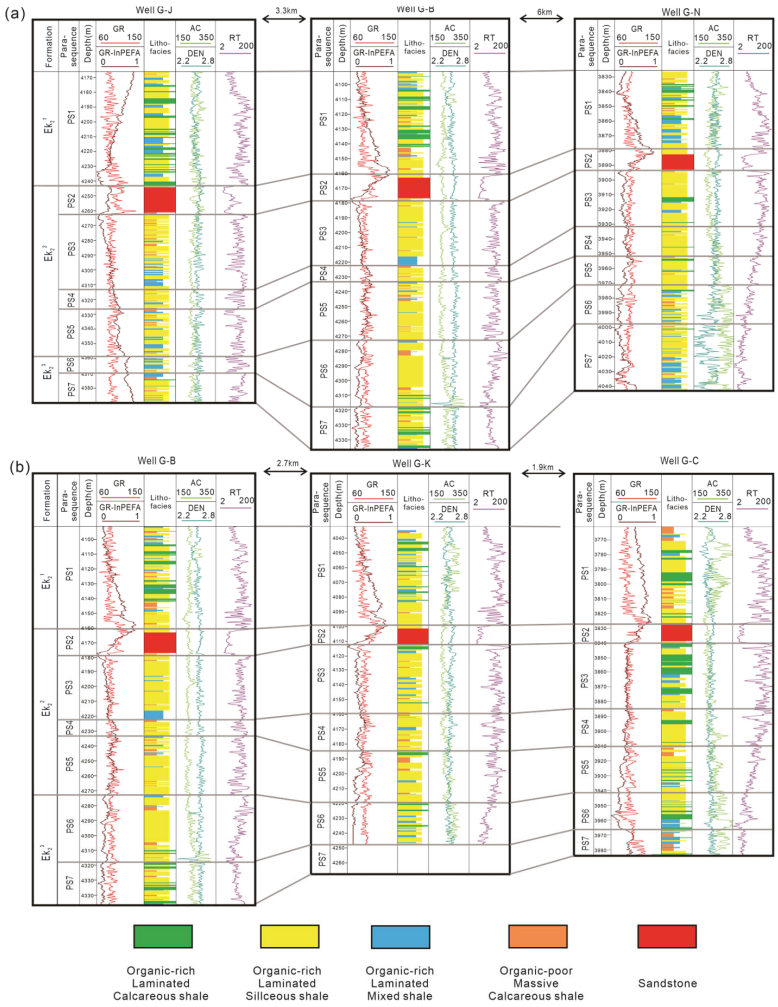

Figure 11. Well sections of predicted lithofacies in Guandong region. The locations of the two well sections are shown in Figure 1b. Well sections in the (**a**) east–west and (**b**) north–south direction.

Table 1. Mineral composition and rock mechanic parameters in different lithofacies in the Ek_2.

Well	Depth (m)	Lithofacies	Quartz (Vol,%)	Feldspar (Vol,%)	Calcite (Vol,%)	Dolomite (Vol,%)	Clay (Vol,%)	Analcite (Vol,%)	TOC (Vol,%)	Mineral Brittleness Index	Elastic Modulus (MPa)	Poisson's Ratio	Mechanical Brittleness Index
G-A	2925.5	MC	18	15	20	11	15	20	1.90	49.91	28.32	0.18	58.17
G-A	2937.6	LM	12	14	14	5	13	22	20.30	35.89	16.14	0.32	19.71
G-A	2955.5	LS	14	18	4	7	13	29	15.68	38.97	18.84	0.35	16.22
G-A	2966.0	LC	13	11	15	33	7	10	11.22	51.92	26.16	0.29	34.34
G-A	2974.0	LC	9	6	4	44	10	15	11.52	51.29	26.40	0.26	39.42
G-A	2999.4	LS	28	53	8	0	4	0	6.66	47.89	16.58	0.21	42.51
G-A	3012.5	LS	20	14	3	0	14	48	0.70	50.12	23.47	0.19	51.91
G-A	3025.1	LS	15	25	11	5	10	25	9.34	43.57	24.73	0.27	37.38
G-A	3032.0	LM	15	14	12	25	12	15	7.61	50.22	27.32	0.21	51.53
G-A	3032.2	LC	13	10	4	38	10	17	7.62	53.75	21.65	0.22	44.91
G-A	3073.8	LM	13	12	2	25	17	17	12.97	43.99	22.31	0.27	33.87
G-A	3187.2	LM	13	22	5	21	18	6	16.26	38.83	15.08	0.32	20.13
G-A	3197.1	LM	22	19	8	18	22	8	2.53	49.12	18.00	0.20	46.43
G-A	3209.0	LS	13	28	5	8	19	0	25.78	28.38	9.97	0.37	6.74
G-A	3281.2	LS	17	20	5	0	26	30	2.69	40.02	15.17	0.25	33.44
G-A	3288.2	MC	16	13	16	20	19	16	0.81	50.18	24.31	0.21	48.00
G-A	3297.8	LC	12	8	8	40	9	8	14.38	50.51	26.33	0.19	54.66

5. Discussion

5.1. Evaluation Parameters of Shale Oil Sweet Spots

5.1.1. Oil-Bearing Capacity

High oil saturation is an important indicator of shale oil enrichment. In shale oil reservoir research, total organic carbon (TOC), chloroform-extractable bitumen "A", and Rock-Eval pyrolysis parameters S_1 and S_2 are commonly utilized as crucial evaluation parameters to distinguish the oil-bearing characteristics of different lithofacies. Due to the abundance of organic-rich laminated layers, three laminated shales (TOC > 2%) in Ek_2 are all considered to be effective source rocks [58]. Based on the crossplot of TOC and S_2 data from well G-A, a strong positive correlation is observed between oil saturation and organic abundance (Figure 12b). The LS and LM lithofacies contain higher organic content, indicating good to excellent hydrocarbon generation potential. The LC lithofacies exhibits a fair to good hydrocarbon generation potential, whereas the MC lithofacies, with fewer organic-rich laminated layers, shows a lower hydrocarbon generation potential, ranging from poor to fair.

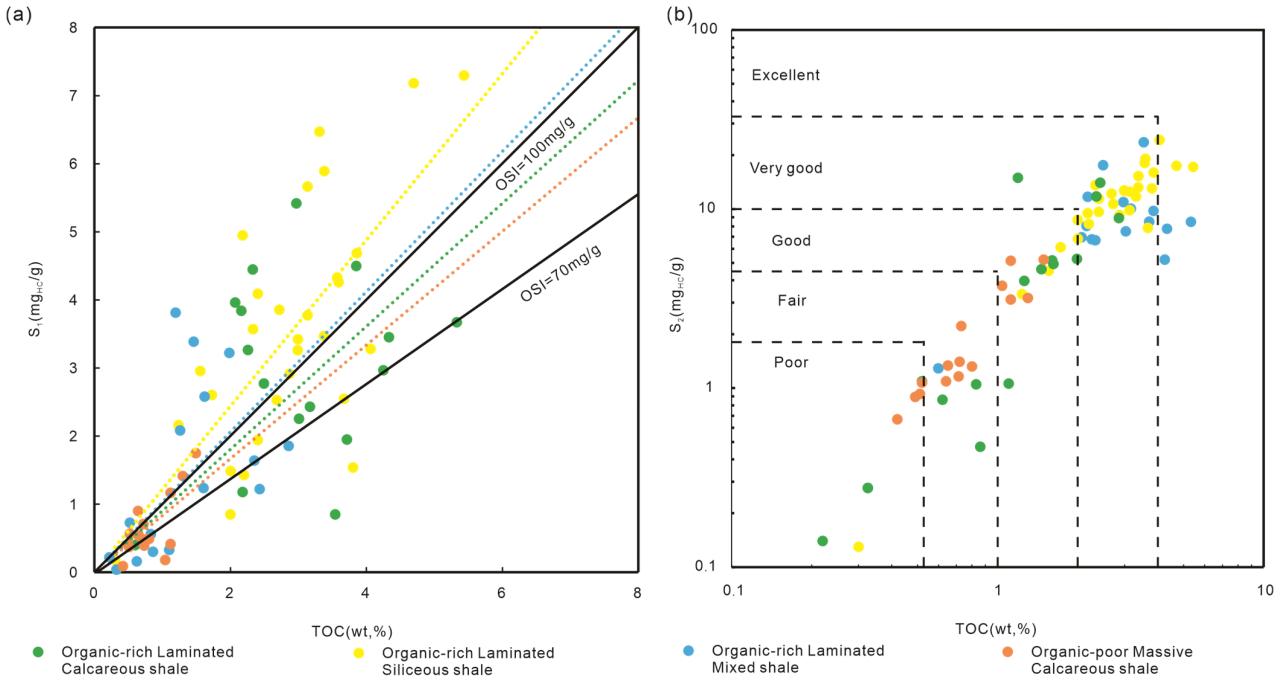

Figure 12. Crossplots of different hydrocarbon generation content and TOC: (**a**) the free hydrocarbon (S_1) content and TOC (with fitting line); (**b**) the kerogen-derived hydrocarbon (S_2) content and TOC.

5.1.2. Reservoir Properties

Pores and fractures, as the main storage space in shale, determine the reservoir's physical properties. Various methods are available to study pore structures, and different measurement techniques offer diverse scales of analysis. Integrating the LNP, MIP, and NMR experiments allows for a comprehensive characterization of the pores across different scales. The comprehensive characterization of pore sizes indicates there is pronounced heterogeneity in the pore distribution characteristics among the different shale lithofacies. The proportion of macropores in the LS lithofacies is higher than 35%, which indicates that the intergranular pores of quartz, feldspar, and other minerals cause siliceous lithofacies to have higher reservoir performance. The macropores in the LC lithofacies are well developed, which may be caused by the dissolution of calcite by acidic fluid generated during the development of intergranular pores and the thermal evolution of dolomite. The complex composition of LM lithofacies, with the deposition of calcareous, siliceous, and clay laminae, contributes to the pronounced heterogeneity in pore size distribution. In addition to the complex mineral composition, the development of micropores, mesopores, and

macropores in the LM lithofacies can also be attributed to the clay mineral transformation processes and organic matter thermal evolution. Unlike the abundant microfractures found in laminated shale, the massive shale exhibits limited development of microfractures. The MC lithofacies has a higher abundance of 5 nm–10 nm mesopores and demonstrates the poorest pore connectivity of the four lithofacies. Based on the comprehensive analysis of pore size distribution maps and porosity data measured from nuclear magnetic resonance (NMR) and mercury intrusion porosimetry (MIP), it is evident that the LS lithofacies exhibits the most favorable reservoir properties, followed by the LC lithofacies, and then the LM lithofacies. Conversely, the MC lithofacies exhibits the poorest reservoir properties among the four lithofacies.

5.1.3. Oil Fluidity

Due to the characteristics of fine-grained deposition, a high proportion of clay minerals, and self-generation and self-storage, some hydrocarbons in shale oil reservoirs are adsorbed into source rocks during pyrolysis. Due to the crossover effect, the fluidity of shale oil becomes a critical aspect in sweet spot evaluation. In previous studies, the dynamic oil coefficient OSI (the ratio of S_1 to TOC) has mostly been used to represent the movable efficiency of shale oil [59]. Based on the experience gained from shale oil exploitation in North America, an OSI greater than 100 mg/g indicates high mobility and high exploitation potential. Due to the shallow burial depth of well G-A, the lower Ro values result in relatively low OSI values. Therefore, an OSI value greater than 70 mg/g is considered indicative of the occurrence of a shale oil crossover effect, suggesting that the reservoir has the potential for industrial production. The crossplot of S_1 and TOC for the four lithofacies reveals that the LS and LM lithofacies exhibit OSI values exceeding 100 mg/g, while the LC and MC lithofacies show relatively smaller OSI values, with an average OSI ranging from 70 mg/g to 100 mg/g (Figure 12a). Under the influence of mineral composition and sedimentary structure, the LS and LM lithofacies have the best oil fluidity, while LC lithofacies and MC lithofacies have relatively poor oil fluidity, but all four lithofacies have recoverable potential.

5.1.4. Fracability

The extremely low porosity and permeability of shale oil reservoirs necessitate the use of hydraulic fracturing as a crucial exploitation technique. The integration of shale oil geology and engineering research has become increasingly important in identifying sweet spots for oil exploitation. A comprehensive characterization of reservoir fracability can be achieved by studying the mechanical and mineralogical properties of different lithofacies. In the evaluation of brittleness in Ek_2 shale, the brittle minerals include calcite, dolomite, quartz, feldspar, and analcime, while the ductile minerals consist of clay minerals and organic matter. By normalizing the volume fractions of organic matter and inorganic minerals, a more comprehensive representation of the influence of organic matter on reservoir brittleness can be achieved. By comparing the indices of mechanical brittleness and mineral brittleness for different lithofacies, a clear positive correlation is observed between the two parameters (R^2 = 0.8), indicating that the mechanical properties of shale are influenced by mineral composition and structure (Figure 13). Due to variations in the development density of organic-rich clay laminations, different lithofacies exhibit distinct differences in their brittleness index values. Specifically, the calcareous shale demonstrates higher values for the brittleness index, while the siliceous and mixed lithofacies exhibit relatively lower values. The shale fracability of Ek_2 is in the order of MC lithofacies, LC lithofacies, LM lithofacies, and LS lithofacies.

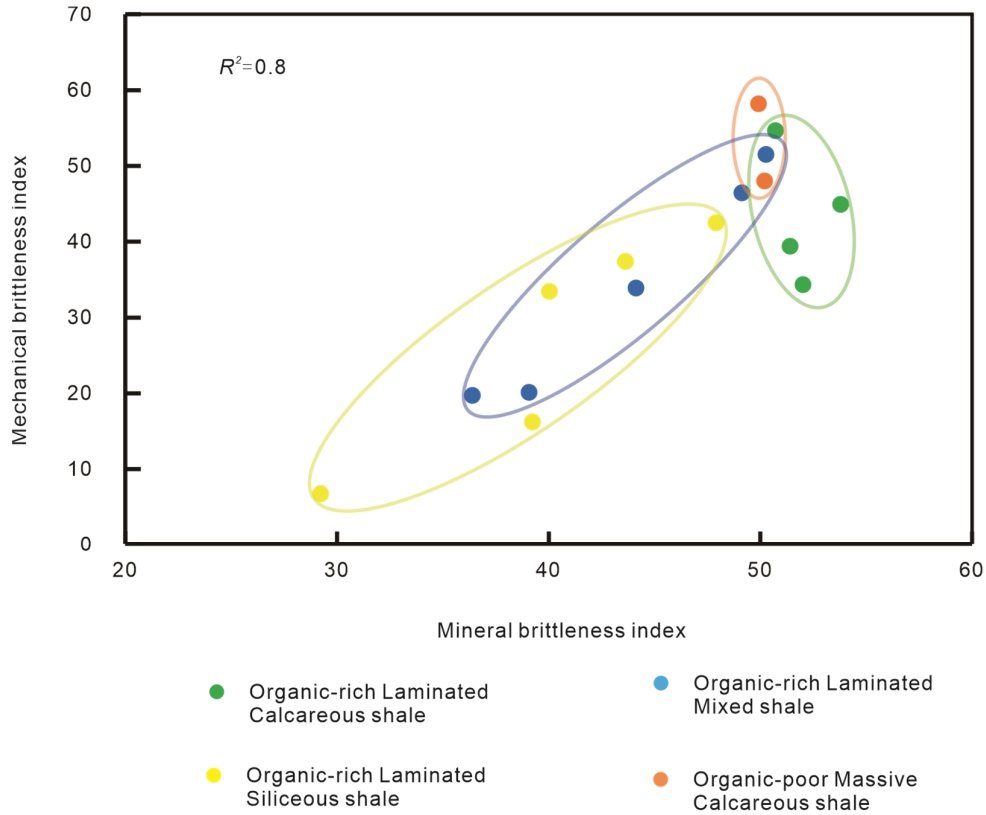

Figure 13. Crossplot of the mechanical brittleness index and the mineral brittleness index.

The sweet spots in shale oil reservoirs are intricately linked with reservoir oil-bearing capacity, reservoir properties, oil fluidity, and fracability. Therefore, in this comprehensive sweet spot evaluation, a multi-parameter equal-weight quantitative evaluation approach was employed. Sweet spot evaluation scores (ES) for the four lithofacies were computed by applying a 25% weighted summation to the normalized TOC, porosity, OSI, and mechanical brittleness index using Equation (3). The evaluation parameters are presented in Table 2. Two levels of sweet spots were identified. Type I includes LC lithofacies (ES of 0.60) and LS lithofacies (ES of 0.75), while type II consists of LM lithofacies (ES of 0.49).

$$ES = \Sigma a_i \cdot P_j, \tag{3}$$

here, ES is the evaluation score; a_i is the weight of the parameter; P_j is the normalized parameter.

Table 2. Evaluation parameters and scores for different lithofacies in the Ek_2.

Lithofacies	Toc (wt%)	OSI (mg/g)	Porosity (%)	Mechanical Brittleness Index	ES
LC	3.2	95.1	4.08	43.33	0.60
LS	3.6	119.4	4.98	31.37	0.75
LM	3.21	102.5	3.44	34.33	0.49
MC	0.82	85.3	2.08	53.09	0.25

5.2. Sweet Spot Distribution and Prediction

In contrast to the stable deposition of thick layers in marine shales, the rapid lithofacies changes in lacustrine basin shales pose challenges for sweet spot prediction. Some researchers have adopted the approach of using a weighted combination of multiple parameters to calculate the sweet spot index and conduct predictive evaluations of sweet

spots [40,60]. However, in regions lacking relevant core data and production information, the implementation of this parameter stacking method can be challenging due to the absence of crucial data, leading to relatively low accuracy in the identification of sweet spots. Lithofacies, as a coupled product of tectonics, sedimentation, and diagenesis, can serve as a substitute for various sweet spot parameters in reservoir sweet spot evaluation. Moreover, the sedimentary laws can be used to enhance the predictive accuracy between wells. Different lithofacies exhibit distinct rock physics properties due to variations in mineral composition. Therefore, by relying on the differences in well log responses among different lithofacies, the accurate prediction of shale lithofacies can be achieved based on high-resolution logging data. Compared to traditional manual log interpretation for lithofacies identification, MRGC technology can reveal multi-dimensional lithofacies–electrical relationships, enabling efficient and precise lithofacies prediction. Based on the MRGC method, lithofacies prediction research was conducted on 12 wells in the Guandong region.

Based on the consideration of sedimentation and diagenesis, the vertical and horizontal distribution of the sweet spots are predicted (Figures 14 and 15). The primary type I sweet spot in Ek_2^1 is LC lithofacies. During the PS1 parasequence, the climate was arid, leading to a lowering of the lake level and an increase in water salinity. As a result, a significant amount of carbonate minerals was deposited. The lithofacies deposited during this period exhibit favorable reservoir properties, oil fluidity, oil generation potential, and excellent fracturability.

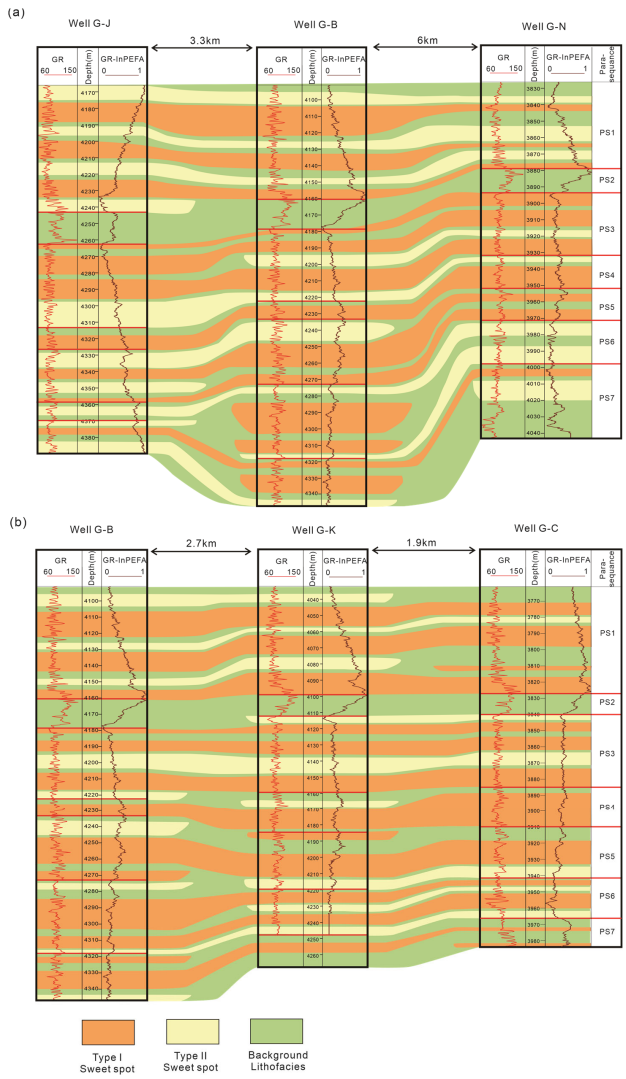

Figure 14. Well sections of sweet spots in the Guandong region. The location of the two well sections is shown in Figure 1b. Well sections in the (**a**) east–west and (**b**) north–south direction.

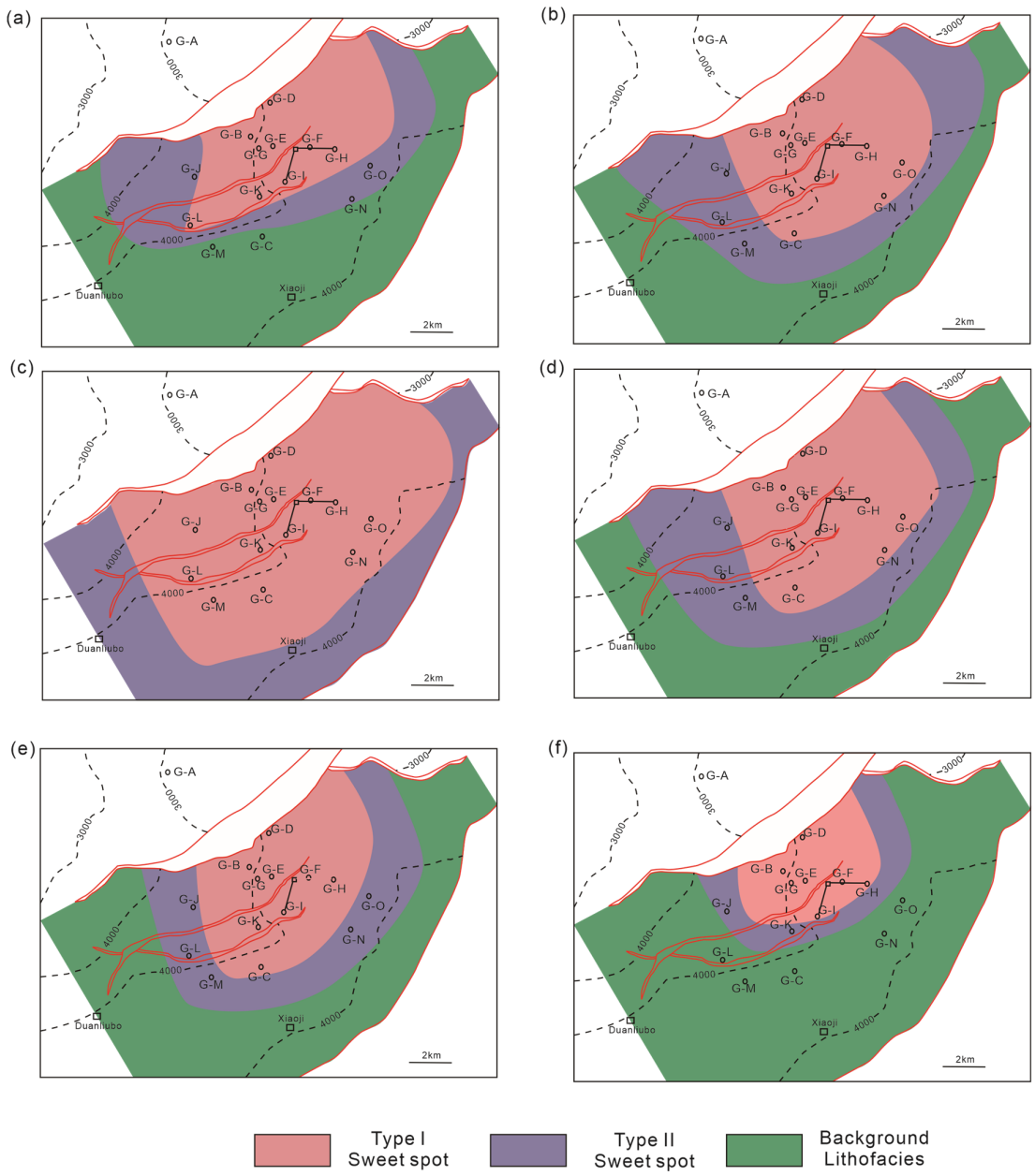

Figure 15. Map of the distribution of sweet spots of different parasequences in the Guandong region. (**a**) PS1; (**b**) PS3; (**c**) PS4; (**d**) PS5; (**e**) PS6; (**f**) PS7.

The type I sweet spot in Ek_2^2 is predominantly composed of LS lithofacies. During the parasequences of PS5 to PS3, the climate tended to be humid, resulting in a significant influx of freshwater into the lake basin, leading to a decrease in water salinity and deepening of the water body (Figure 15c–e). Consequently, a significant amount of organic matter was deposited in the lake basin. The sedimentary environment experienced multiple cycles of fluctuations and an ample supply of detrital materials, which facilitated the extensive development of LS lithofacies. During this period, the lithofacies exhibit excellent reservoir properties, oil fluidity, and oil generation potential, along with moderate fracturability. During the parasequences of PS7 to PS6, as the lake basin deepened and the input of terrigenous debris gradually decreased, the fluctuating climate led to a gradual reduction in the deposition of LS lithofacies, and the sedimentation of LC lithofacies increased. These two lithofacies together constitute the type I sweet spot during the Ek_2^3 period. In the Ek_2 period, the sedimentation of the entire Cangdong Sag was centered in the northwest part of the Guandong region. During the PS7–PS4 period, the lake basin deepened, whereas

during the PS4–PS1 period, the lake basin became more shallow. Consequently, throughout these sedimentary processes, the sweet spot areas exhibited a ring-like expansion and contraction pattern, as seen in the planar view.

6. Conclusions

This paper presents the lithofacies-based evaluation and prediction of sweet spots in Ek_2 of the Cangdong Sag. Firstly, based on core analysis, XRD analysis, FE-SEM observations, and the organic geochemical parameters obtained from rock pyrolysis experiments, Ek_2 was categorized into four lithofacies: organic-rich laminated calcareous shale (LC), organic-rich laminated siliceous shale (LS), organic-rich laminated mixed shale (LM), and organic-poor massive calcareous shale (MC).

Subsequently, the organic geochemical parameters obtained from rock pyrolysis experiments were used to investigate the oil-bearing capacity and oil fluidity. The characterization of pore structure and reservoir physical properties was conducted using LNP, MIP, and NMR experiments. The reservoir fracability was evaluated using the brittleness index obtained from triaxial stress tests. Taking into account geological and engineering factors, two types of sweet spots were classified: LS and LC for type I, and LM for type II.

Finally, the distribution of sweet spots was indicated by predicting the distribution of lithofacies. The sweet spots differ slightly for the different sedimentary periods. In $Ek_2{}^1$, the optimum lithofacies are LC lithofacies, whereas in $Ek_2{}^2$, there is a shift to LS lithofacies. In $Ek_2{}^3$, the sweet spots are distributed in both LC and LS lithofacies. The distribution of sweet spots is jointly controlled by climate cyclicity and changes in lacustrine basin water bodies. The dominant distribution characteristics of different lithofacies at vertical intervals and the ring-like distribution patterns in the planar view can provide theoretical guidance for the next stage in shale oil exploration. The findings of this study represent valuable insights for sweet spot research in lacustrine shale oil reservoirs.

The distribution of sweet spots is closely related to the distribution of lithofacies, but the heterogeneity and rapid lithofacies changes in lacustrine shale pose significant challenges for sweet spot evaluation. Therefore, clarifying the sedimentary and diagenetic patterns of lacustrine shale in guiding the prediction of lithofacies and sweet spots in areas without wells represents the future direction of research.

Author Contributions: Conceptualization, C.L.; methodology, P.M.; software, G.L.; validation, C.M.; formal analysis, Y.Z.; investigation, C.M.; resources, W.H.; data curation, W.H.; writing—original draft preparation, Y.Z.; writing—review and editing, C.L.; visualization, Y.Z.; supervision, C.L.; project administration, C.L.; funding acquisition, C.L. All authors have read and agreed to the published version of the manuscript.

Funding: This research was funded by the National Natural Science Foundation of China (NSFC), grant number 41972142 and 42172153.

Data Availability Statement: Not applicable.

Conflicts of Interest: The authors declare no conflict of interest.

References

1. Chalmers, G.R.; Bustin, R.M.; Power, I.M. Characterization of Gas Shale Pore Systems by Porosimetry, Pycnometry, Surface Area, and Field Emission Scanning Electron Microscopy/Transmission Electron Microscopy Image Analyses: Examples from the Barnett, Woodford, Haynesville, Marcellus, and Doig Units. *AAPG Bull.* **2012**, *96*, 1099–1119. [CrossRef]
2. Liang, C.; Cao, Y.; Jiang, Z.; Wu, J.; Guoqi, S.; Wang, Y. Shale Oil Potential of Lacustrine Black Shale in the Eocene Dongying Depression: Implications for Geochemistry and Reservoir Characteristics. *AAPG Bull.* **2017**, *101*, 1835–1858. [CrossRef]
3. Zhang, W.; Xie, L.; Yang, W.; Qin, Y.; Peng, P. Micro Fractures and Pores in Lacustrine Shales of the Upper Triassic Yanchang Chang7 Member, Ordos Basin, China. *J. Pet. Sci. Eng.* **2017**, *156*, 194–201. [CrossRef]
4. Zou, Y.-R.; Sun, J.-N.; Li, Z.; Xu, X.; Li, M.; Peng, P. Evaluating Shale Oil in the Dongying Depression, Bohai Bay Basin, China, Using the Oversaturation Zone Method. *J. Pet. Sci. Eng.* **2018**, *161*, 291–301. [CrossRef]
5. He, W.; Liu, Y.; Wang, D.; Lei, D.; Liu, G.; Gao, G.; Huang, L.; Qi, Y. Geochemical Characteristics and Process of Hydrocarbon Generation Evolution of the Lucaogou Formation Shale, Jimsar Depression, Junggar Basin. *Energies* **2022**, *15*, 2331. [CrossRef]

6. Yang, W.; Zuo, R.; Wang, X.; Song, Y.; Jiang, Z.; Luo, Q.; Zhai, J.; Wang, Q.; Zhang, C.; Zhang, Z. Sensitivity of Lacustrine Stromatolites to Cenozoic Tectonic and Climatic Forcing in the Southern Junggar Basin, NW China: New Insights from Mineralogical, Stable and Clumped Isotope Compositions. *Palaeogeogr. Palaeoclimatol. Palaeoecol.* **2019**, *514*, 109–123. [CrossRef]
7. Lazar, O.R.; Bohacs, K.M.; Macquaker, J.H.S.; Schieber, J.; Demko, T.M. Capturing Key Attributes of Fine-Grained Sedimentary Rocks In Outcrops, Cores, and Thin Sections: Nomenclature and Description Guidelines. *J. Sediment. Res.* **2015**, *85*, 230–246. [CrossRef]
8. Talbot, M.R. The Origins of Lacustrine Oil Source Rocks: Evidence from the Lakes of Tropical Africa. *Geol. Soc. Lond. Spec. Publ.* **1988**, *40*, 29–43. [CrossRef]
9. Ma, P.; Lin, C.; Li, G.; Dong, C.; Jiang, L.; Du, X.; Ren, M.; Liu, W.; Zhao, Z.; Yuan, Y.; et al. Lithofacies Characteristics and Sweet Spot Distribution of Lacustrine Shale Oil: A Case Study from the Dongying Depression, Bohai Bay Basin, China. *Lithosphere* **2022**, *2022*, 3135681. [CrossRef]
10. Zhi, D.; Xiang, B.; Zhou, N.; Li, E.; Zhang, C.; Wang, Y.; Cao, J. Contrasting Shale Oil Accumulation in the Upper and Lower Sweet Spots of the Lacustrine Permian Lucaogou Formation, Junggar Basin, China. *Mar. Pet. Geol.* **2023**, *150*, 106178. [CrossRef]
11. Zou, C.; Yang, Z.; Zhu, R.; Wu, S.; Fu, J.; Lei, D.; Hou, L.; Lin, S.; Pan, S. Geologic Significance and Optimization Technique of Sweet Spots in Unconventional Shale Systems. *J. Asian Earth Sci.* **2019**, *178*, 3–19. [CrossRef]
12. Chen, Z.; Jiang, W.; Zhang, L.; Zha, M. Organic Matter, Mineral Composition, Pore Size, and Gas Sorption Capacity of Lacustrine Mudstones: Implications for the Shale Oil and Gas Exploration in the Dongying Depression, Eastern China. *AAPG Bull.* **2018**, *102*, 1565–1600. [CrossRef]
13. Hill, R.J.; Jarvie, D.M.; Zumberge, J.; Henry, M.; Pollastro, R.M. Oil and Gas Geochemistry and Petroleum Systems of the Fort Worth Basin. *AAPG Bull.* **2007**, *91*, 445–473. [CrossRef]
14. Cai, J.; Cai, C.; Lu, L.; Jiang, Q.; Ma, X.; He, J. Hydrous Pyrolysis of Source Rocks with Different Maturity in Dongying Sag, Bohai Bay Basin, China: Implications for Shale Oil Exploration and Development. *Energies* **2023**, *16*, 6219. [CrossRef]
15. Zhang, S.; Liu, H.; Liu, Y.; Wang, Y.; Wang, M.; Bao, Y.; Hu, Q.; Li, Z.; Zhang, S.; Yao, S.; et al. Main Controls and Geological Sweet Spot Types in Paleogene Shale Oil Rich Areas of the Jiyang Depression, Bohai Bay Basin, China. *Mar. Pet. Geol.* **2020**, *111*, 576–587. [CrossRef]
16. Li, X.; Chen, K.; Li, P.; Li, J.; Geng, H.; Li, B.; Li, X.; Wang, H.; Zang, L.; Wei, Y.; et al. A New Evaluation Method of Shale Oil Sweet Spots in Chinese Lacustrine Basin and Its Application. *Energies* **2021**, *14*, 5519. [CrossRef]
17. Liu, S.; Liu, Y.; Zhang, X.; Guo, W.; Kang, L.; Yu, R.; Sun, Y. Geological and Engineering Integrated Shale Gas Sweet Spots Evaluation Based on Fuzzy Comprehensive Evaluation Method: A Case Study of Z Shale Gas Field HB Block. *Energies* **2022**, *15*, 602. [CrossRef]
18. Tang, X.; Jiang, Z.; Huang, H.; Jiang, S.; Yang, L.; Xiong, F.; Chen, L.; Feng, J. Lithofacies Characteristics and Its Effect on Gas Storage of the Silurian Longmaxi Marine Shale in the Southeast Sichuan Basin, China. *J. Nat. Gas Sci. Eng.* **2016**, *28*, 338–346. [CrossRef]
19. Yang, W.; Zuo, R.; Jiang, Z.; Chen, D.; Song, Y.; Luo, Q.; Wang, Q.; Zhu, H. Effect of Lithofacies on Pore Structure and New Insights into Pore-Preserving Mechanisms of the over-Mature Qiongzhusi Marine Shales in Lower Cambrian of the Southern Sichuan Basin, China. *Mar. Pet. Geol.* **2018**, *98*, 746–762. [CrossRef]
20. Liang, C.; Zhang, J.; Zhu, J.; Wang, W.; Guo, H.; Tan, Q.; Zhao, J.; Luo, H. The Influence of Continental Mixosedimentite Sedimentation on Shale Oil Sweet Spot: A Case Study on the Permian Lucaogou Formation in the Jimsar Sag of the Junggar Basin, NW China. *Front. Earth Sci.* **2023**, *10*, 929768. [CrossRef]
21. Saggaf, M.M.; Nebrija, E.L. A Fuzzy Logic Approach for the Estimation of Facies from Wire-Line Logs. *AAPG Bull.* **2003**, *87*, 1223–1240. [CrossRef]
22. Jungmann, M.; Kopal, M.; Clauser, C.; Berlage, T. Multi-Class Supervised Classification of Electrical Borehole Wall Images Using Texture Features. *Comput. Geosci.* **2011**, *37*, 541–553. [CrossRef]
23. Liu, B.; Wang, H.; Fu, X.; Bai, Y.; Bai, L.; Jia, M.; He, B. Lithofacies and Depositional Setting of a Highly Prospective Lacustrine Shale Oil Succession from the Upper Cretaceous Qingshankou Formation in the Gulong Sag, Northern Songliao Basin, Northeast China. *AAPG Bull.* **2019**, *103*, 405–432. [CrossRef]
24. Li, Y.; Li, Z.-X.; Wang, D.-D.; Song, G.-Z.; Lv, D.-W.; Lusheng-Yin; Liu, H.-Y.; Xu, C.-H.; Kong, F.-F.; Han, Q.-Y. Continental Lacustrine Fine-Grained Lithofacies, Assemblage and Geological Significance of Unconventional Petroleum: A Case Study of the Paleogene of the 4th Member of the Shahejie Formation in the Jiyang Depression. *Energy Explor. Exploit.* **2023**, *41*, 62–83. [CrossRef]
25. Liu, B.; Zhao, X.; Fu, X.; Yuan, B.; Bai, L.; Zhang, Y.; Ostadhassan, M. Petrophysical Characteristics and Log Identification of Lacustrine Shale Lithofacies: A Case Study of the First Member of Qingshankou Formation in the Songliao Basin, Northeast China. *Interpretation* **2020**, *8*, SL45–SL57. [CrossRef]
26. Ou, C.; Li, C.; Rui, Z.; Ma, Q. Lithofacies Distribution and Gas-Controlling Characteristics of the Wufeng–Longmaxi Black Shales in the Southeastern Region of the Sichuan Basin, China. *J. Pet. Sci. Eng.* **2018**, *165*, 269–283. [CrossRef]
27. Chen, S.; Zhang, S.; Wang, Y.; Tan, M. Lithofacies Types and Reservoirs of Paleogene Fine-Grained Sedimentary Rocks Dongying Sag, Bohai Bay Basin, China. *Pet. Explor. Dev.* **2016**, *43*, 218–229. [CrossRef]

28. Raeesi, M.; Moradzadeh, A.; Doulati Ardejani, F.; Rahimi, M. Classification and Identification of Hydrocarbon Reservoir Lithofacies and Their Heterogeneity Using Seismic Attributes, Logs Data and Artificial Neural Networks. *J. Pet. Sci. Eng.* **2012**, *82–83*, 151–165. [CrossRef]
29. Wang, G.; Carr, T.R.; Ju, Y.; Li, C. Identifying Organic-Rich Marcellus Shale Lithofacies by Support Vector Machine Classifier in the Appalachian Basin. *Comput. Geosci.* **2014**, *64*, 52–60. [CrossRef]
30. Zhao, Z.; Su, S.; Shan, X.; Li, X.; Zhang, J.; Jing, C.; Ren, H.; Li, A.; Yang, Q.; Xing, J. Lithofacies Identification of Shale Reservoirs Using a Tree Augmented Bayesian Network: A Case Study of the Lower Silurian Longmaxi Formation in the Changning Block, South Sichuan Basin, China. *Geoenergy Sci. Eng.* **2023**, *221*, 211385. [CrossRef]
31. Kim, J. Lithofacies Classification Integrating Conventional Approaches and Machine Learning Technique. *J. Nat. Gas Sci. Eng.* **2022**, *100*, 104500. [CrossRef]
32. Zhao, X.; Zhou, L.; Pu, X.; Jin, F.; Han, W.; Shi, Z.; Chen, C.; Jiang, W.; Guan, Q.; Xu, J.; et al. Theories, technologies and practices of lacustrine shale oil exploration and development: A case study of Paleogene Kongdian Formation in Cangdong sag, Bohai Bay Basin, China. *Pet. Explor. Dev.* **2022**, *49*, 707–718. [CrossRef]
33. Fang, Z.; Chen, S.; Pu, X.; Yan, J.; Chen, X. Control of Sedimentary Environment on the Lithofacies of Lacustrine Fine-Grained Sedimentary Rocks in the Second Member of the Kongdian Formation in the Cangdong Sag, Bohai Bay Basin, China. *Geol. J.* **2022**, *57*, 2321–2345. [CrossRef]
34. Hao, F.; Zou, H.; Gong, Z.; Deng, Y. Petroleum Migration and Accumulation in the Bozhong Sub-Basin, Bohai Bay Basin, China: Significance of Preferential Petroleum Migration Pathways (PPMP) for the Formation of Large Oilfields in Lacustrine Fault Basins. *Mar. Pet. Geol.* **2007**, *24*, 1–13. [CrossRef]
35. Zhao, X.; Pu, X.; Yan, J.; Jin, F.; Shi, Z.; Chai, G.; Han, W.; Liu, Y.; Jiang, W.; Chen, C.; et al. Cycles of Fine-Grained Sedimentation and Their Influences on Organic Matter Distribution in the Second Member of Paleogene Kongdian Formation in Cangdong Sag, Bohai Bay Basin, East China. *Pet. Explor. Dev.* **2023**, *50*, 534–546. [CrossRef]
36. Deng, Y.; Chen, S.; Pu, X.; Yan, J.; Cui, J. Formation Mechanism and Environmental Evolution of Fine-Grained Sedimentary Rocks from the Second Member of Kongdian Formation in the Cangdong Sag, Bohai Bay Basin. *Oil Gas Geol.* **2020**, *41*, 811–823, 890. [CrossRef]
37. Zhao, X.; Zhou, L.; Pu, X.; Jin, F.; Jiang, W.; Xiao, D.; Han, W.; Shi, Z. Development and exploration practice of the concept of hydrocarbon accumulation in rifted-basin troughs: A case study of Paleogene Kongdian Formation in Cangdong sag, Bohai Bay Basin. *Pet. Explor. Dev.* **2018**, *45*, 1166–1176. [CrossRef]
38. Pu, X.; Zhou, L.; Han, W.; Zhou, J.; Wang, W.; Zhang, W.; Chen, S.; Shi, Z.; Liu, S. Geologic Features of Fine-Grained Facies Sedimentation and Tight Oil Exploration: A Case from the Second Member of Paleogene Kongdian Formation of Cangdong Sag, Bohai Bay Basin. *Pet. Explor. Dev.* **2016**, *43*, 26–35. [CrossRef]
39. Zhao, X.; Pu, X.; Han, W.; Zhou, L.; Shi, Z.; Chen, S.; Xiao, D. A New Method for Lithology Identification of Fine Grained Deposits and Reservoir Sweet Spot Analysis: A Case Study of Kong 2 Member in Cangdong Sag, Bohai Bay Basin, China. *Pet. Explor. Dev.* **2017**, *44*, 524–534. [CrossRef]
40. Zhao, X.; Pu, X.; Jin, F.; Chen, C.; Shi, Z.; Chai, G.; Han, W.; Jiang, W.; Guan, Q.; Zhang, W. Enrichment Law and Favorable Exploration Area of Shale-Type Shale Oil in Huanghua Depression. *ACTA Pet. Sin.* **2023**, *44*, 158–175. [CrossRef]
41. Xin, B.; Hao, F.; Liu, X.; Han, W.; Xu, Q.; Guo, P.; Tian, J. Quantitative Evaluation of Pore Structures within Micron-Scale Laminae of Lacustrine Shales from the Second Member of the Kongdian Formation in Cangdong Sag, Bohai Bay Basin, China. *Mar. Pet. Geol.* **2022**, *144*, 105827. [CrossRef]
42. Liu, Z.; Huang, C.; Algeo, T.J.; Liu, H.; Hao, Y.; Du, X.; Lu, Y.; Chen, P.; Guo, L.; Peng, L. High-Resolution Astrochronological Record for the Paleocene-Oligocene (66–23 Ma) from the Rapidly Subsiding Bohai Bay Basin, Northeastern China. *Palaeogeogr. Palaeoclimatol. Palaeoecol.* **2018**, *510*, 78–92. [CrossRef]
43. Espitalie, J.; Madec, M.; Tissot, B.; Mennig, J.J.; Leplat, P. Source Rock Characterization Method for Petroleum Exploration. In *Offshore Technology Conference*; Offshore Technology Conference: Houston, TX, USA, 1977. [CrossRef]
44. Barrett, E.P.; Joyner, L.G.; Halenda, P.P. The Determination of Pore Volume and Area Distributions in Porous Substances. I. Computations from Nitrogen Isotherms. *J. Am. Chem. Soc.* **1951**, *73*, 373–380. [CrossRef]
45. Bhattacharya, S.; Carr, T.R.; Pal, M. Comparison of Supervised and Unsupervised Approaches for Mudstone Lithofacies Classification: Case Studies from the Bakken and Mahantango-Marcellus Shale, USA. *J. Nat. Gas Sci. Eng.* **2016**, *33*, 1119–1133. [CrossRef]
46. Wheeler, H.E. Baselevel, Lithosphere Surface, and Time-Stratigraphy. *Geol. Soc. Am. Bull.* **1964**, *75*, 599–610. [CrossRef]
47. Yuan, R.; Zhu, R.; Qu, J.; Wu, J.; You, X.; Sun, Y.; Zhou (Nancy), Y. Utilizing Integrated Prediction Error Filter Analysis (INPEFA) to Divide Base-Level Cycle of Fan-Deltas: A Case Study of the Triassic Baikouquan Formation in Mabei Slope Area, Mahu Depression, Junggar Basin, China. *Open Geosci.* **2018**, *10*, 79–86. [CrossRef]
48. Tissot, B.P.; Pelet, R.; Ungerer, P. Thermal History of Sedimentary Basins, Maturation Indices, and Kinetics of Oil and Gas Generation. *AAPG Bull.* **1987**, *71*, 1445–1466. [CrossRef]
49. Applied Source Rock Geochemistry. In *The Petroleum System—From Source to Trap*; American Association of Petroleum Geologists: Tulsa, OK, USA, 1994; pp. 93–120. [CrossRef]
50. Jarvie, D.M. Shale Resource Systems for Oil and GasPart 2—Shale-Oil Resource Systems. In *Shale Reservoirs—Giant Resources for the 21st Century*; American Association of Petroleum Geologists: Tulsa, OK, USA, 2012. [CrossRef]

51. Loucks, R.G.; Ruppel, S.C. Mississippian Barnett Shale: Lithofacies and Depositional Setting of a Deep-Water Shale-Gas Succession in the Fort Worth Basin, Texas. *AAPG Bull.* **2007**, *91*, 579–601. [CrossRef]
52. Loucks, R.G.; Reed, R.M.; Ruppel, S.C.; Hammes, U. Spectrum of Pore Types and Networks in Mudrocks and a Descriptive Classification for Matrix-Related Mudrock Pores. *AAPG Bull.* **2012**, *96*, 1071–1098. [CrossRef]
53. Brunauer, S.; Emmett, P.H.; Teller, E. Adsorption of Gases in Multimolecular Layers. *J. Am. Chem. Soc.* **1938**, *60*, 309–319. [CrossRef]
54. Sing, K.S.W. Reporting Physisorption Data for Gas/Solid Systems with Special Reference to the Determination of Surface Area and Porosity (Recommendations 1984). *Pure Appl. Chem.* **1985**, *57*, 603–619. [CrossRef]
55. Ma, B.; Hu, Q.; Yang, S.; Yin, N.; Qiao, H.; Zhang, T.; Meng, M. Multiple Approaches to Quantifying the Effective Porosity of Lacustrine Shale Oil Reservoirs in Bohai Bay Basin, East China. *Geofluids* **2020**, *2020*, 8856620. [CrossRef]
56. Rouquerol, J.; Avnir, D.; Fairbridge, C.W.; Everett, D.H.; Haynes, J.M.; Pernicone, N.; Ramsay, J.D.F.; Sing, K.S.W.; Unger, K.K. Recommendations for the Characterization of Porous Solids (Technical Report). *Pure Appl. Chem.* **1994**, *66*, 1739–1758. [CrossRef]
57. Han, W.; Dou, Y.; Li, H.; Zhang, W.; Shi, Z.; Dong, J. Optimization and Application of Brittleness Evaluation Methods for Continental Organic-Rich Shale: A Case Study of the 2nd Member of Kongjiadian Formation, Cangdong Sag, Bohai Bay Basin. *Oil Drill. Prod. Technol.* **2022**, *44*, 191–198. [CrossRef]
58. Zou, C.; Dong, D.; Yang, H.; Wang, Y.; Huang, J.; Wang, S.; Fu, C. Conditions of Shale Gas Accumulation and Exploration Practices in China. *Nat. Gas Ind.* **2011**, *31*, 26–39. [CrossRef]
59. Jarvie, D.M.; Hill, R.J.; Ruble, T.E.; Pollastro, R.M. Unconventional Shale-Gas Systems: The Mississippian Barnett Shale of North-Central Texas as One Model for Thermogenic Shale-Gas Assessment. *AAPG Bull.* **2007**, *91*, 475–499. [CrossRef]
60. Han, W.; Zhao, X.; Jin, F.; Pu, X.; Chen, S.; Mu, L.; Zhang, W.; Shi, Z.; Wang, H. Sweet Spot Evaluation and Exploration Practice of Lacustrine Shale Oil of the Second Member of Kongdian Formation in Cangdong Sag, Bohai Bay Basin. *Pet. Explor. Dev.* **2021**, *48*, 900–910. [CrossRef]

Disclaimer/Publisher's Note: The statements, opinions and data contained in all publications are solely those of the individual author(s) and contributor(s) and not of MDPI and/or the editor(s). MDPI and/or the editor(s) disclaim responsibility for any injury to people or property resulting from any ideas, methods, instructions or products referred to in the content.